Supporting Information:

Molecular dynamics analysis of fast-spreading severe acute respiratory syndrome coronavirus 2 variants and their effects in the interaction with human angiotensin-converting enzyme 2

Anacleto Silva de Souza[1], Vitor Martins de Freitas Amorim[1], Gabriela D A Guardia[2], Felipe R C dos Santos[2,3], Filipe F dos Santos[2,4], Robson Francisco de Souza[1], Guilherme de Araujo Juvenal[4], Yihua Huang[5], Pingju Ge[5], Yinan Jiang[5], Coco Li[5], Prajwal Paudel[5], Henning Ulrich[4], Pedro A F Galante[2], Cristiane Rodrigues Guzzo[1,*]

[1]Department of Microbiology, Institute of Biomedical Sciences, University of São Paulo, São Paulo, Brazil.
[2]Centro de Oncologia Molecular, Hospital Sírio Libanes, São Paulo, Brazil.
[3]Programa Interunidades em Bioinformática, University of São Paulo, São Paulo, Brazil.
[4]Department of Biochemistry, Institute of Chemistry, University of São Paulo, São Paulo, Brazil.
[5]ACROBiosystems Inc., 8 N. Hongda Rd., Beijing Economic-Technological Development Area, Beijing, 100176, China.

* Corresponding author
E-mail: crisguzzo@usp.br and crisguzzo@gmail.com

To whom correspondence should be addressed:

Cristiane R. Guzzo, Ph.D, Department of Microbiology, Institute of Biomedical Sciences, University of São Paulo, Av. Prof. Lineu Prestes, 1374, Cidade Universitária, 5508-900, São Paulo/SP, Brazil, +55 11 3091-7298; E-mail: crisguzzo@usp.br

Keywords: SARS-CoV-2 variants, binding affinity, molecular dynamics, transcriptome analysis, SPR assay, COVID-19.

Materials and Methods **S1**
Molecular dynamics (MD) simulations S2
Molecular mechanics combined with Poisson-Boltzmann surface area (MM-PBSA) S3
Protein-protein binding assays using surface plasmon resonance (SPR) S4
Genes and splicing isoforms expression analyses S5

Supplementary text **S6**
Solvent-accessible surface area (SASA) analysis S6
Molecular mechanics combined with Poisson-Boltzmann surface area (MM-PBSA) studies S6
Hydrogen bonding occupancy analysis S7
Cross-correlation analysis S8

Figures S1 - S17. **S10**

Tables S1 - S9. **S27**

Materials and Methods

Molecular dynamics (MD) simulations

The initial coordinates for RBD/hACE2 complex were obtained from the Protein Data Bank (PDB ID 6M0J, resolution 2.45 Å)[1] and prepared using the UCSF Chimera[2] by removing co-crystallized hetero groups (except Zn^{2+}) and water molecules. RBD mutations were obtained from a site-directed mutation in wild-type RBD using the Maestro software (academic v. 2020-1) [3]. From the ACE2/RBD complex structure, protonation states of ionizable residues were computed in an aqueous implicitly environment at pH 7.0 from the Maestro software academic v. 2020-1 [3] using PROPKA module [4]. In all protein complexes, then, all glutamic and aspartic residues were represented as unprotonated; all glutamic residues were kept with neutral charge; arginine and lysine residues were assumed with a positive charge; the N- and C-terminal were converted to charged groups. In hACE2, H34, H195, H345, H374, H378, and H417 were designed as a δ-tautomer; H228, H239, H241, H265, H373, H401, H505, H535 and H540 were modeled as an ε-tautomer. In RBD, H519 was designed as a δ-tautomer. The system conditions were prepared using GROMACS v. 5.1.4[5–8] with the OPLS-AA force field[9]. We used the Swiss-Param web-based service to build the Zn^{2+} topology[10]. All systems were explicitly solvated with *TIP3P* water models in a triclinic box (81.06 X 91.06 X 135.02 $Å^3$), neutralized keeping NaCl concentration of 150 mM and minimized until a maximum force of 10.0 $kJ.mol^{-1}$ or 5,000 steps. The systems were consecutively equilibrated in isothermal-isochoric (NVT). To equilibrate the system, it was relaxed during a 5000 ps annealing, in which the temperature was increased from 300 to 330 K each 500 ps, and isothermal-isobaric (1 bar; NpT) ensembles at 310 K for 1000 ps. MD simulations in the NpT ensemble were carried out for 100 ns in a periodic box considering the minimum distance of 10 Å between any protein atom and box walls. The Zn^{2+} positions were restricted throughout the simulations. In order to confirm the convergence of the simulation between hACE2 and RBD of the Alpha (B.1.1.7) and Gamma (P.1) variants and wild type (WT), we simulated 300 ns of these complexes, using the same conditions used in the simulations of 100 ns. Backbone root-mean-square deviation (RMSD), and backbone root-mean-square fluctuation

(RMSF) calculations were performed using GROMACS. Hydrogen bonding occupancies (%) were calculated in virtual molecular dynamics (VMD; v. 1.9.1). Analysis of C_α cross-correlated displacements were performed using the R-based package Bio3d[11]. The correlations ranged from -1 (anti-correlated motions) to 1 (correlated motions). Principal component analysis and SASA were calculated using the GROMACS package. Using molecular dynamics simulation trajectories, we determined the average structure representing backbone hACE (2373 atoms) and backbone RBD (1791 atoms) and calculated correlation matrix fitting non-mass weighted. From the calculated correlation matrix, we determined eigenvalues diagonalizing the 7119x7119 matrix (representing backbone hACE2) and 5373x5373 matrix (representing backbone RBD). The first and second eigenvalues are shown in **Table S9**. From the PC1, we observed 100 snapshots corresponding to MD trajectories obtained from the first component (**supplementary movies S1** and **S2**). We used first and second components to verify trajectory scores of hACE2 and also RBD^{WT} and their variants (**Figure S6**).

Molecular mechanics combined with Poisson-Boltzmann surface area (MM-PBSA)

The molecular mechanics combined with the Poisson-Boltzmann surface area (MM-PBSA) was calculated using the Kumari method[12], which approximates the solvation contribution to a continuous solvent model and approximates ΔG to a thermodynamic cycle by modeling a continuous solvent in the Poisson-Boltzmann area. The charges, radius and concentration of positive ions were +1, 0.95 Å and 0.15 M, respectively. The charges, radius and concentration of negative ions were -1, 1.81 Å and 0.15 M, respectively. The dielectric constant of the solute, solvent and vacuum was 32, 80 and 1, respectively. The radius of the solvent probe was 1.4 Å. The method for mapping the grid was sp14 and the model used to build the dielectric and ionic limits was smol. In the free-energy calculation, we considered for the non-polar solvent, the surface tension, probe radius and energy cut-off of 0.023 $kJ.mol^{-1}.Å^{-2}$, 1.4 Å, 3.85 $kJ.mol^{-1}$, respectively. Non-polar attractive contribution term was determined by the probe radius, the density of solvent in the grid and the cubic

grid spacing for the calculation of the volume integrals of 1.20 Å, 0.03 $Å^3$ and 0, 7 Å, respectively. The time interval analyzed was 1 ns.

Protein-protein binding assays using surface plasmon resonance (SPR)

The experimental K_D (M^{-1}) of the SARS-CoV-2 Spike/hACE2 complex were obtained by surface plasmon resonance (SPR) assays using a Biacore 8K system (GE Healthcare). The assays as well as protein cloning, expression and purification were performed by the ACROBiosystems company. SARS-CoV-2 Spike constructions are fused to a 10 polyhistidine tag at the C-terminus of the recombinant proteins. Four different constructions of the Spike RBD as well as four constructions of recombinant Spike trimers were used in SPR assays: the RBD^{WT} (residues 319 to 537, SPD-C52H3, ACROBiosystems); the $RBD^{B.1.1.7(Alpha)}$ (N501Y, residues 319 to 537, SPD-C52Hn, ACROBiosystems); the $RBD^{B.1.351(beta)}$ (K417N, E484K N501Y, residues 319 to 537; SPD-C52Hp, ACROBiosystems); the $RBD^{P.1(Gamma)}$ (K417T, E484K N501Y, residues 319 to 537; SPD-C52Hr, ACROBiosystems); Spike $trimer^{WT}$ (residues 16 to 1213 with the following mutations at: R683A, R685A, F817P, A892P, A899P, A942P, K986P, V987P; SPN-C52H9, ACROBiosystems); Spike $trimer^{B.1.1.7(Alpha)}$ (residues 16 to 1213 with the following mutations at: R683A, R685A, F817P, A892P, A899P, A942P, K986P, V987P and additional mutations at: H69-V70del, Y144del, N501Y, A570D, D614G, P681H, T716I, S982A, D1118H; SPN-C52H6, ACROBiosystems); Spike $trimer^{B.1.351(Beta)}$ (residues 16 to 1213 with the following mutations at: R683A, R685A, F817P, A892P, A899P, A942P, K986P, V987P and additional mutations at: L18F, D80A, D215G, L242-A243-L244del, R246I, K417N, E484K, N501Y, D614G, A701V; SPN-C52Hk, ACROBiosystems); Spike $trimer^{P.1(Gamma)}$ (residues 16 to 1213 with the following mutations at: R683A, R685A, F817P, A892P, A899P, A942P, K986P, V987P and additional mutations at: L18F, T20N, P26S, D138Y, R190S, K417T, E484K, N501Y, D614G, H655Y, T1027I, V1176F; SPN-C52Hg, ACROBiosystems). In Spike trimer constructions the proline substitutions (F817P, A892P, A899P, A942P, K986P, V987P) were introduced to stabilize the trimeric prefusion state of SARS-CoV-2 Spike protein and alanine substitutions (R683A and R685A) were introduced to abolish the furin cleavage site. The human ACE2 (residues from 18 - 740) is fused to a Fc tag at the C-terminus of

the recombinant protein (MW 110 kDa; AC2-H5257, ACROBiosystems), in which hACE2 is in a dimer form.

Anti-Human IgG (Fc) antibody was diluted at 25 µg/mL in an immobilization buffer (10 mM Sodium Acetate pH 5.0 present in GE Human Antibody Capture Kit, catalog number 29234600 - Cytia), to be covalently immobilized to a CM5 sensor chip (GE Healthcare, catalog number BR100530 - Cytiva) via their amine groups using the human antibody capture kit (29234600, GE Healthcare). Immobilization processes were performed using a flow rate of Anti-Human IgG (Fc) antibody of 10 $\mu L.min^{-1}$ during 360 s, where obtained response unit (RU) signals were about 7,000-14,000. Human ACE2 with a C-terminal Fc tag was diluted in a running buffer (10 mM HEPES, pH 7.4, 3 mM EDTA, 0.005% Tween-20, 150 mM NaCl). The RU signal obtained was about 150 in the capture hACE2 protein-ligand. After that, serial dilutions of purified recombinant Spike proteins were injected ranging in concentrations (as shown in **Table S7**). Spike proteins were injected at a flow rate of 30 $\mu L.min^{-1}$ during association (120 s) and dissociation (300 s). The chip was regenerated using a regeneration buffer (3M magnesium chloride, present in GE Human Antibody Capture Kit, GE) at a flow rate of 20 $\mu L.min^{-1}$ in 30 s. The resulting data were fitted to a 1:1 binding model using Biacore Evaluation Software (GE Healthcare).

Genes and splicing isoforms expression analyses

To investigate the expression profiles of *ACE2*, *FURIN* and *TMPRSS2*, we gathered Transcripts Per Million (TPM)-normalized gene expression data of 16,705 samples from 32 healthy tissues directly at The Genotype-Tissue Expression (GTEx) portal (https://gtexportal.org/). Subject phenotype information (gender and age) of all analyzed individuals were also collected at the GTEx portal and used for posterior data stratification. To investigate isoform-based expression levels of *ACE2*, we downloaded RNA sequencing datasets from 163 samples (27 tissues) at ENA projects (accession IDs: PRJEB4337; PRJEB6971). To obtain TPM-normalized expression values, the datasets were processed using Kallisto [13] with GENCODE (v37) as reference to the human transcriptome. Boxplots and correlation plots were

generated using local R scripts. Alignment of translated transcripts was performed through clustal W [14] using *ACE2* transcripts from GENCODE (v37) and ORFfinder [15].

Supplementary text

Solvent-accessible surface area (SASA) analysis

Such conformational changes affect the solvent-accessible surface area (SASA) of hACE2 while interacting with RBD^{WT} and its variants (**Figure S4**). In this regard, RBD^{WT} and $RBD^{B.1.351}$ keep SASA values of ~273 and 270 nm², respectively (**Figure S4a,c**). Interacting with $RBD^{B.1.1.7}$, hACE2 decreases SASA value from ~278 to 263 nm² but when it interacts with $RBD^{P.1}$, SASA value changes from 270 to 260 nm² (**Figure S4a,c**). In general, RBD variants and WT did not present significant differences in SASA along MD trajectory, presenting values ranging between 107.0 and 109.2 nm^2 (**Figure S4b,d**). Taken together, SASA values are associated with conformational states of hACE2 due to closing of its active site mediated by RBD and its variants. In order to confirm the convergence of the simulation between hACE2 and RBD of the Alpha (B.1.1.7) and Gamma (P.1) variants and wild type (WT), we simulated 300 ns of these complexes, using the same conditions used in the simulations of 100 ns (**Figure S15-17**).

Molecular mechanics combined with Poisson-Boltzmann surface area (MM-PBSA) studies

We also compared the binding free energies between Spike RBD of the different B.1.1.7, B.1.351 and P.1 variants with RBD^{WT}, using molecular mechanics combined with Poisson-Boltzmann surface area (MM-PBSA) (**Figure S7** and **Table S6**). Our results have shown that RBD^{WT}, $RBD^{B.1.351}$, $RBD^{P.1}$ and $RBD^{B.1.1.7}$ present values of -1100 ± 85, -1393 ± 84, -1489 ± 78 and -1013 ± 101 kJ/mol, respectively (**Table S6**). Our MM-PBSA data are comparable with values reported in the literature [16,17]. $RBD^{B1.1.7}$ presented binding free energy similar to RBD^{WT}, which we have believed that they present insignificant differences in binding affinity. We noted that, in interactions between hACE2 and different RBD^{WT}, $RBD^{B.1.351}$, $RBD^{P.1}$

and $RBD^{B.1.1.7}$, Coulomb energy term has a better contribution for free energy than remaining terms, having values of -1380 ± 86, -1453 ± 80, -1461 ± 79 and -1285 ± 76 kJ/mol, respectively (**Table S6**). In addition, Van der Waals energy term presented values of -352 ± 341, -368 ± 33, -430 ± 52 and -297 ± 32 kJ/mol, respectively (**Table S6**). The change in free energy of polar solvation calculated by Poisson-Boltzmann equation (Polar) presented a negative contribution for binding free energy, which presented values of 678 ± 87, 472 ± 85, 454 ± 85 and 612 ± 147 kJ/mol, respectively (**Table S6**). The change in the nonpolar interaction energy under the changes in the protein−solvent accessible surface area (SASA) also were determined e presented values of -46 ± 4, -44 ± 4, -52 ± 6 and -42 ± 6 kJ/mol, respectively (**Table S6**). In general, binding free energy ratio between RBD^{WT} and different $RBD^{B.1.351}$, $RBD^{P.1}$ and $RBD^{B.1.1.7}$ presented values in the range from ~0.9-fold to ~1.4-fold, leading us to believe that the observed reduction between hACE2 and RBD of these SARS-CoV-2 variants presented a moderate effect in decreasing binding affinity. Also, we investigated the contribution of each residue to the binding free energy between RBD and hACE2 (**Figure S7**). Interestingly, most contributions are localized on the hACE2/RBD complex interface and are more frequent in the variants.

Hydrogen bonding occupancy analysis

We calculated hydrogen bonding occupancies of residue pairs of each RBD variant/hACE2 interface and compared them with WT (**Table S3**). We noted that there were gains and losses of hydrogen bonding interactions. These results are explained due to different movements of the RBD of these variants, when compared with WT. We observed that residue pairs Q493-sc^{RBD}/E35-sc^{hACE2}, T449-sc^{RBD}/R273-mc^{hACE2}, Y449-sc^{RBD}/D38-sc^{hACE2} , and Y495-sc^{RBD}/E406-sc^{hACE2} kept the hydrogen bonding interactions in hACE2/RBD complex interface, demonstrating that such interactions are relevant in the molecular recognition between hACE2 and RBD. Differently from RBD^{WT}, the three variants gained intramolecular hydrogen bonding interaction between (N or Y)501-sc^{RBD}/G496-mc^{RBD} but lost between pairs K475-sc^{RBD}/E495-sc^{RBD}, Y489-sc^{RBD}/N487-sc^{RBD} and (K/T/N)417-sc^{RBD}/L455-mc^{RBD} (**Table S3**). Interestingly, we also observed that the

$RBD^{P.1}$ presents specific hydrogen bonding between pairs Y501-sc^{RBD}/Q498-sc^{RBD}. Conversely, $RBD^{B.1.1.7}$ presents specific hydrogen bonding interactions between pairs N487-sc^{RBD}/A475-mc^{hACE2}, T500-sc^{RBD}/G354-mc^{hACE2}, Y501-sc^{RBD}/K353-mc^{hACE2} and Y501-sc^{RBD}/Y41-sc^{hACE2}. Comparing hydrogen bonding interactions on the interface of the complexes RBD^{WT}/hACE2 and $RBD^{P.1}$/hACE2, we also observed this interaction between pairs Q498-sc^{RBD}/D38-sc^{hACE2}, T500-sc^{RBD}/D355-sc^{hACE2} and Y489-sc^{RBD}/Y83-sc^{hACE2}. Comparing also the complexes RBD^{WT}/hACE2 and $RBD^{B.1.1.7}$/hACE2, we also observed hydrogen bonding interactions between pairs K417-sc^{RBD}/D30-sc^{hACE2} and K417-sc^{RBD}/H34-sc^{hACE2}. When compared with the hACE2/RBD^{WT} complex, we have seen the hydrogen bonding interactions between pairs K31-sc^{hACE2}/Q493-sc^{RBD}, T500-sc^{RBD}/Y41-sc^{hACE2} and T453-sc^{RBD}/T449-mc^{RBD} in the $RBD^{B.1.351}$/hACE2 and $RBD^{P.1}$/hACE2 complexes (**Table S3**). Also observed in the B.1.1.7 variant, hydrogen bonding interactions have been seen between R482-sc^{RBD}/E489-sc^{RBD} in P.1 and between T453-sc^{RBD} T449-mc^{RBD} in B.1.351 (**Table S3**).

Cross-correlation analysis

We calculated the correlation matrix of the spatial displacements of C_α atoms to study internal motions of the hACE2/RBD^{WT} complex and compared them with different SARS-CoV-2 RBD mutants (**Figure S5** and **Tables S4** and **S5**). This computational strategy assumes the hypothesis that residues, even afar, can influence the interactions of other residues. The residue pairs that present absolute correlated and anti-correlated values of more than 0.8 were considered to have more influence over other complex residues (**Table S5**). As shown in **Tables S4-S5** and **Figure S5**, sets of intermolecular and intramolecular correlation pairs changed between different SARS-CoV-2 RBD mutants and RBD^{WT}. Both correlated and anticorrelated pairs are affected in E1 and E2 regions of RBD variants, mostly in B.1.1.7 (**Figure S5**). The number of intermolecular correlation pairs for RBD^{WT}, $RBD^{B.1.351}$, $RBD^{P.1}$ and $RBD^{B.1.1.7}$ are 21, 8, 135 and 384, respectively (**Table S5**). Among them, only $RBD^{B.1.1.7}$ presented 76 intramolecular negative correlation pairs (**Table S5**). Furthermore, the number of intramolecular positive correlation pairs in hACE2, caused by each RBD, were 3088, 3656, 4160 and 6852, respectively,

showing that they increase the internal motions in the host receptor. Conversely, as shown in **Figure S5 e-h** and **Table S5**, the number of intramolecular positive correlations for RBD^{WT}, $RBD^{B.1.351}$, $RBD^{P.1}$ and $RBD^{B.1.1.7}$ were 436, 466, 458 and 924, respectively. Interestingly, we did not observe intermolecular anti-correlated pairs between different hACE2/RBD complexes (**Table S5**).

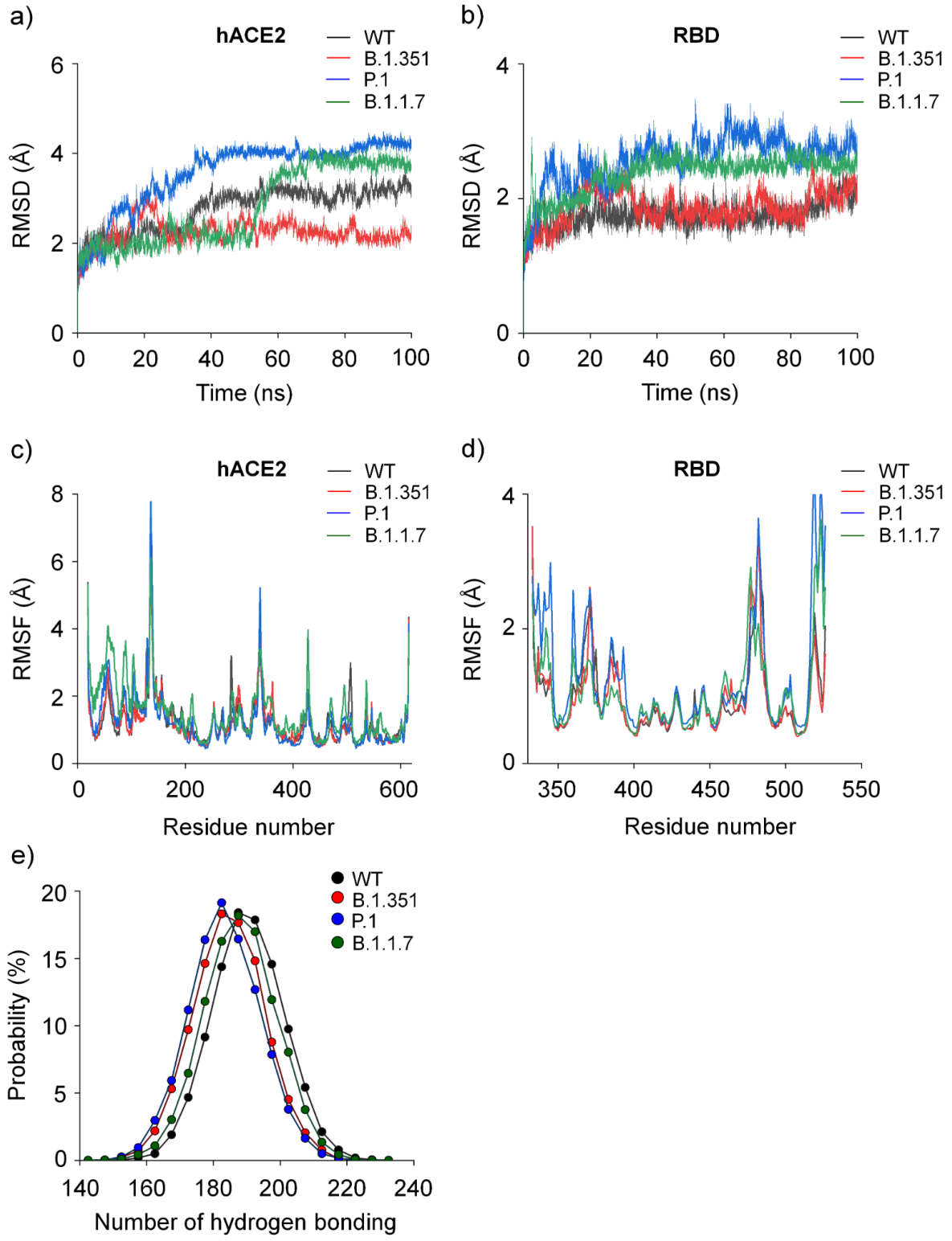

Figure S1.

Structural aspects of the SARS-CoV-2 RBD variants and hACE2. **a)** Backbone root-mean-square deviation (RMSD) of hACE2 in complex with RBD (black color) and RBD variants (red, B.1.351; blue, P.1; green, B.1.1.7). It is an interesting

behavior for the $RBD^{B.1.1.7}$ variant in complex with hACE2 that has a RMSD jump from 2 to 4 Å in ~50 ns. We observed in another independent calculation simulated for 300 ns that there is the same structural behavior after 50 ns (**Figure S15**), converging the calculation in agreement with the dynamics data for 100 ns. We verified that this jump is related to the closing of the hACE2 enzymatic cavity. **b)** Backbone RMSD of RBD (black color) and RBD variants (red, B.1.351; blue, P.1; green, B.1.1.7). **c)** Backbone root-mean-square fluctuation (RMSF) of hACE2 in complex with RBD (black color) and RBD variants (red, B.1.351; blue, P.1; green, B.1.1.7). **d)** Backbone RMSF of RBD (black color) and RBD variants (red, B.1.351; blue, P.1; green, B.1.1.7). **e)** Probability distributions of the number of hydrogen bonding interactions of RBD (black color) and its variants (red, B.1.351; blue, P.1; green, B.1.1.7) in complex with hACE2.

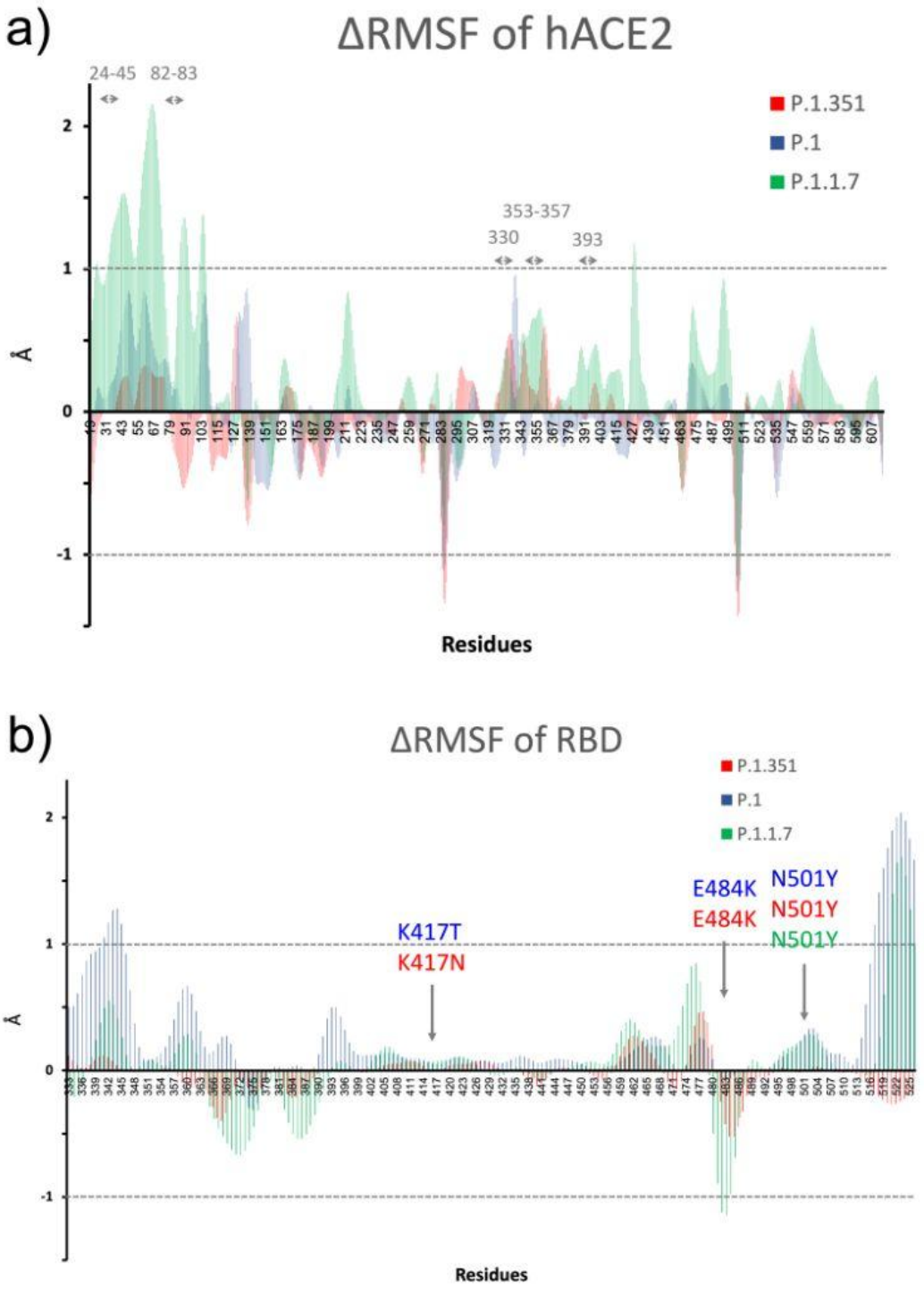

Figure S2. Backbone root-mean-square fluctuation differences of the hACE2 interacting with RBD variants. a) Relative backbone $RMSF^{hACE2}$. **b)** Relative backbone $RMSF^{RBD}$. Both panels **a-b** adopt the hACE2/RBD^{WT} complex as reference.

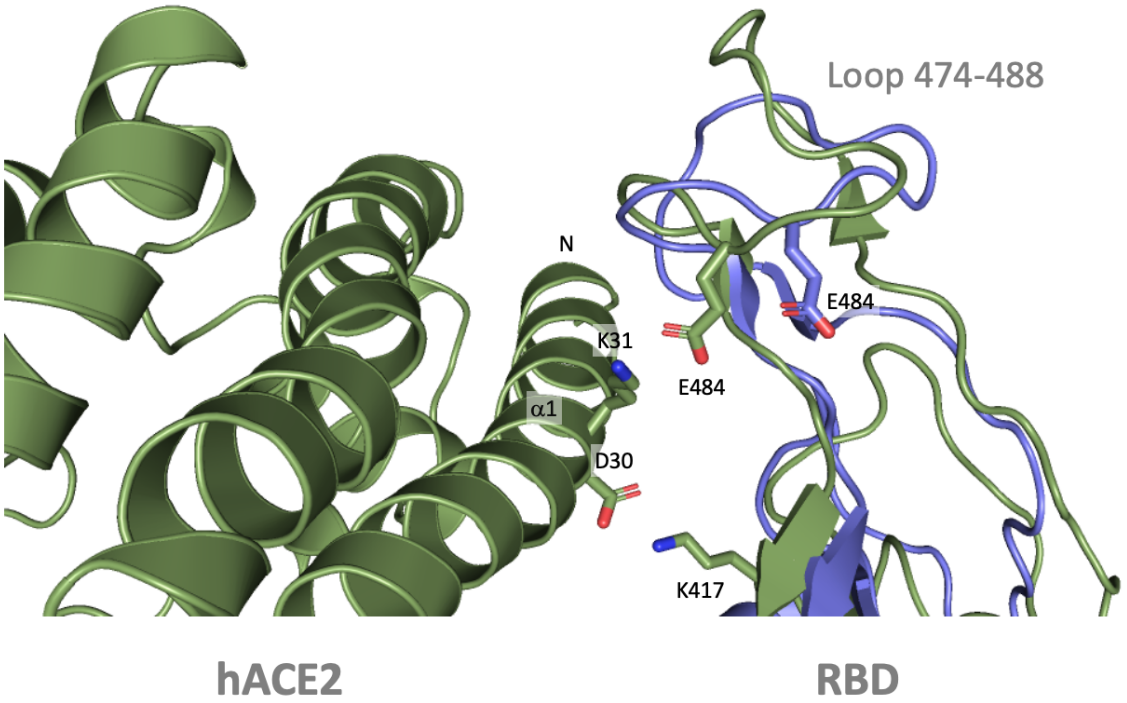

Figure S3. Comparison between modeled hACE2/RBD$^{B.1.1.7}$ (green color) with trimeric Spike RBD$^{B.1.1.7}$ obtained by cryo-electron microscopy (blue color, PDB ID 7MJG [18]).

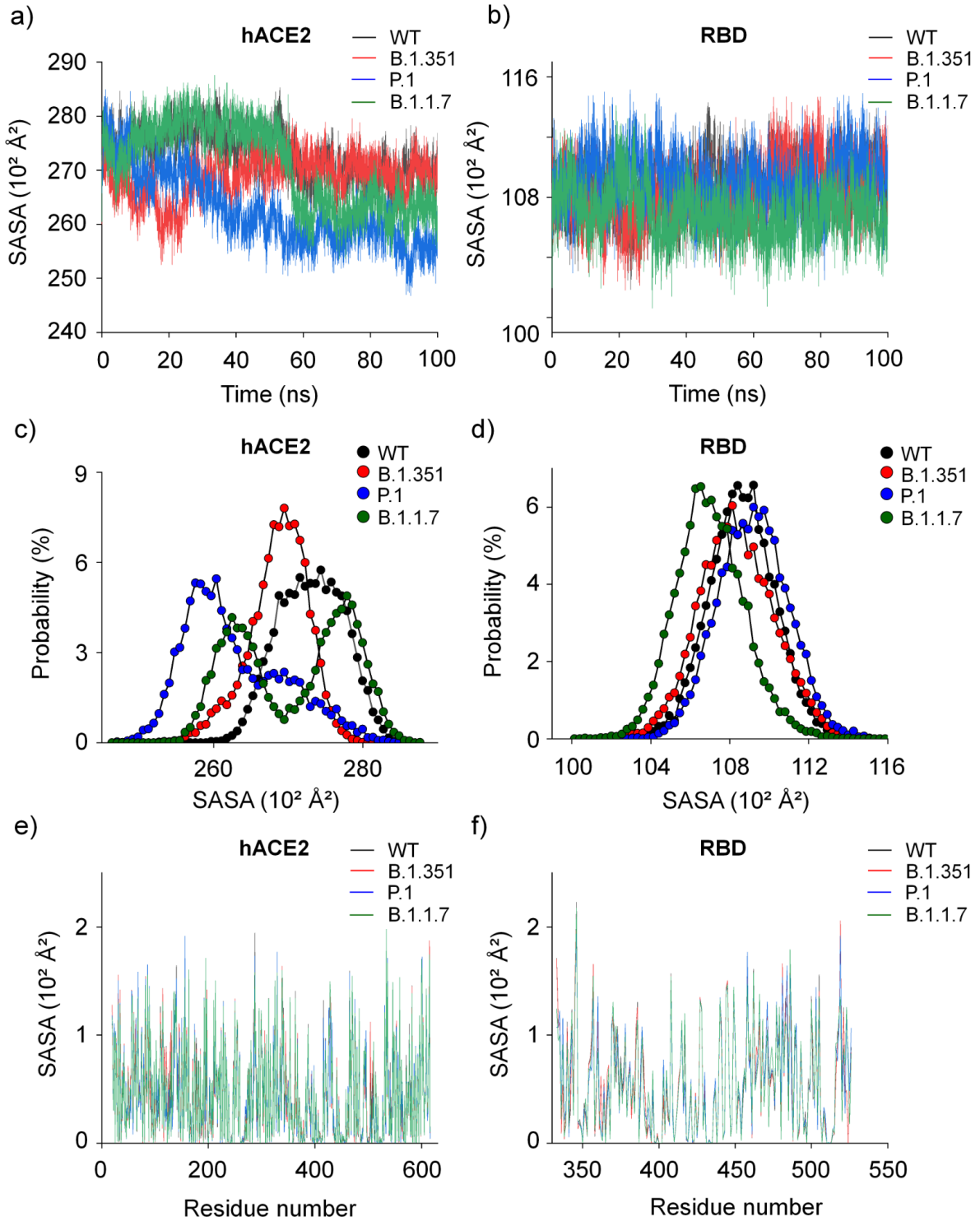

Figure S4. Solvent-accessible surface area (SASA) information of SARS-CoV-2 RBD variants and hACE2. SASA of **a)** hACE2 while interacting with **b)** RBD^{WT} and its variants. **c)** hACE2 and **d)** RBD SASA probability distributions. SASA per residue of **e)** hACE2 in complex with **f)** RBD (black color) and RBD variants (red, B.1.351; blue, P.1; green, B.1.1.7). RBD^{WT} and its variants did not present significant differences in SASA along MD trajectory. However, SASA values presented changes in hACE2,

and such alterations are associated with conformational states of hACE2 due to closing of its active site mediated by RBD and its variants.

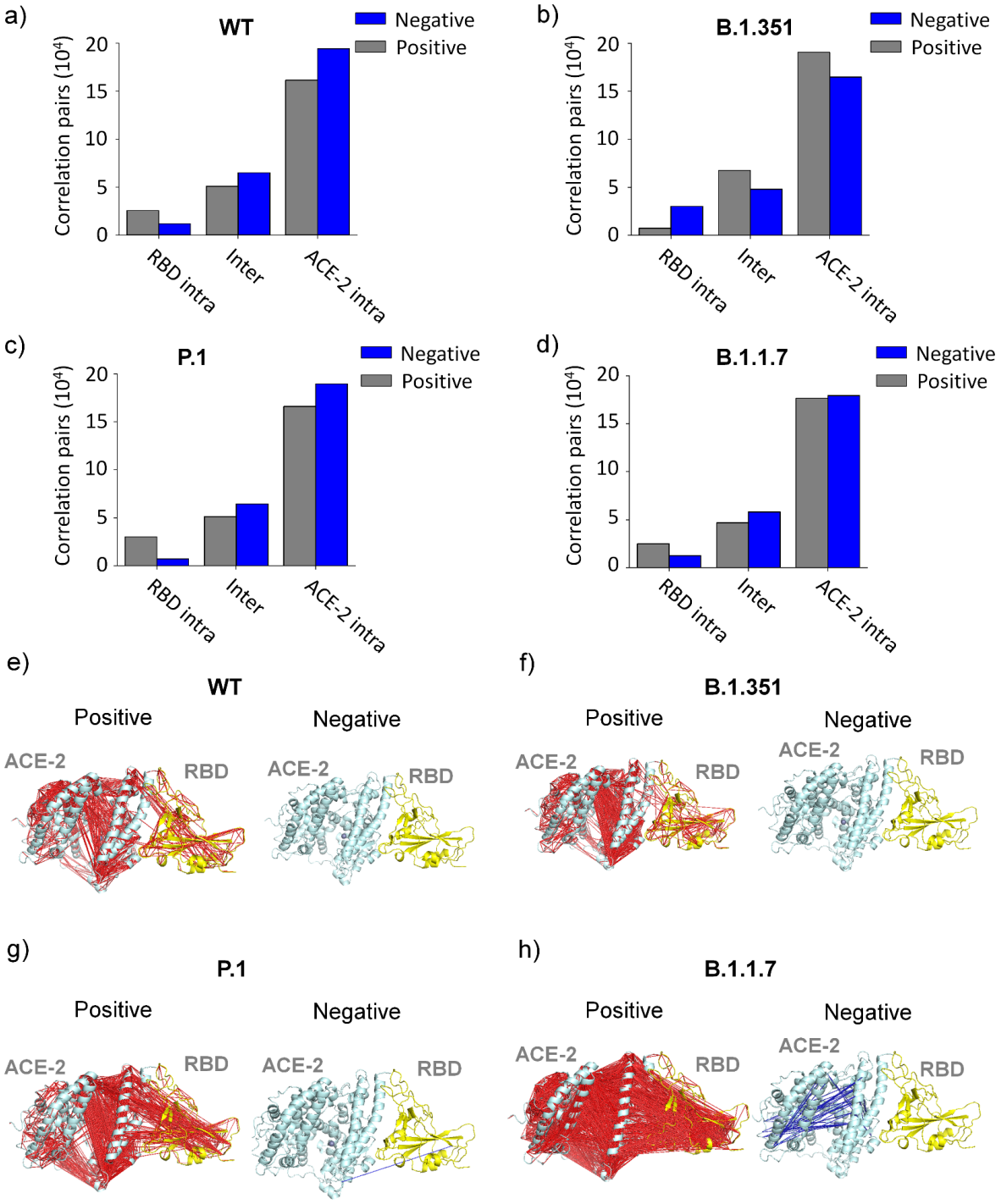

Figure S5. Cross-correlation analysis between SARS-CoV-2 RBD variants and hACE2. Correlation analysis of MD trajectories of RBD variants and WT. panels **a-d** Number of correlation pairs observed in the interaction of RBD^{WT} and their variants with hACE2. Panels **e-h** Pairs of C_α exhibiting correlation higher than 0.8 were

analyzed in the interaction of RBD^{WT} and their variants with hACE2. The red and blue colors represent positive and negative correlations, respectively.

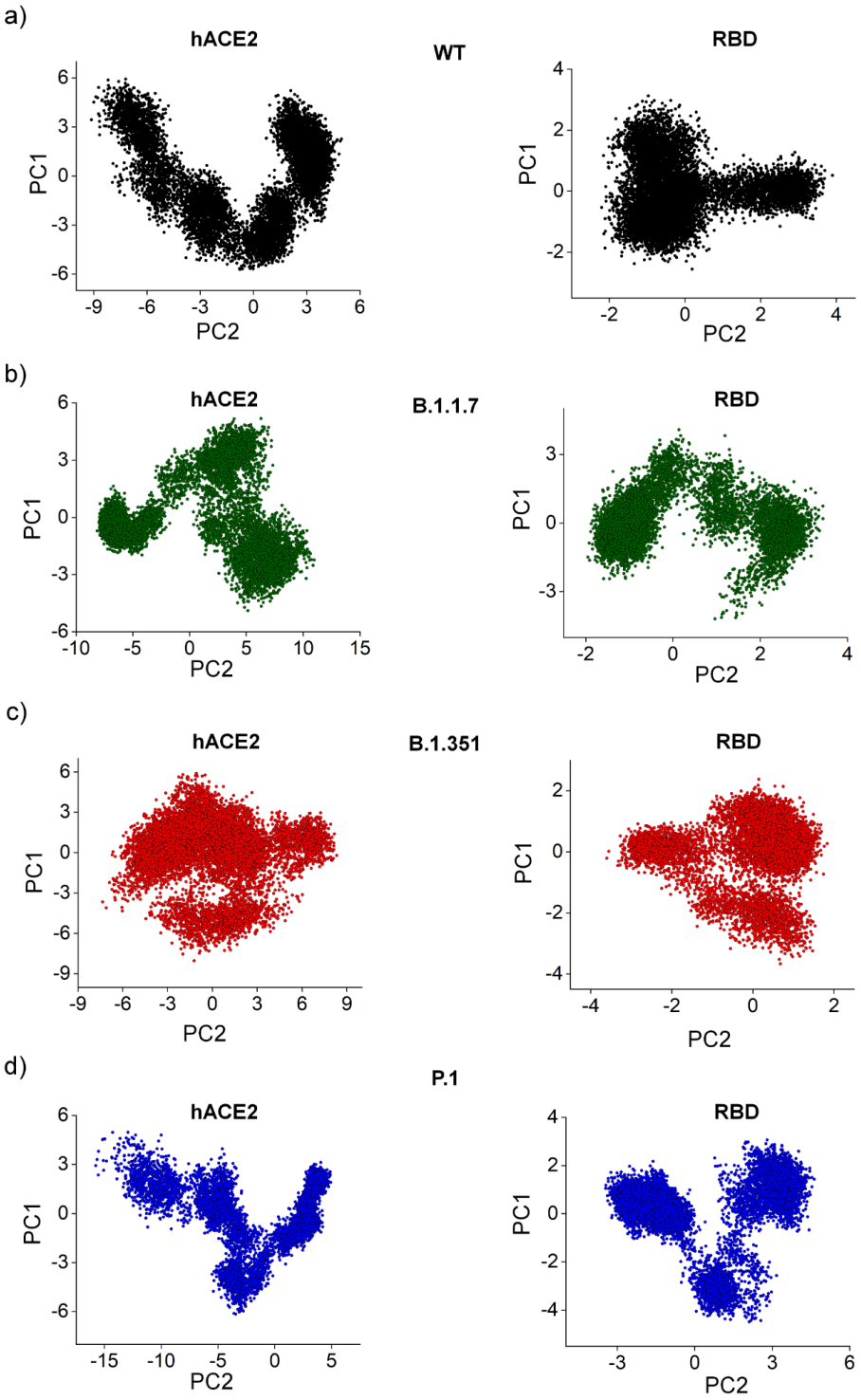

Figure S6. Molecular dynamics trajectories obtained by principal component analysis. Using first and second components, painels a-d show trajectory scores of hACE2 while interacting with **a)** RBD^{WT}, **b)** $RBD^{B.1.1.7}$, **c)** $RBD^{B.1.351}$, and **d)** $RBD^{P.1}$.

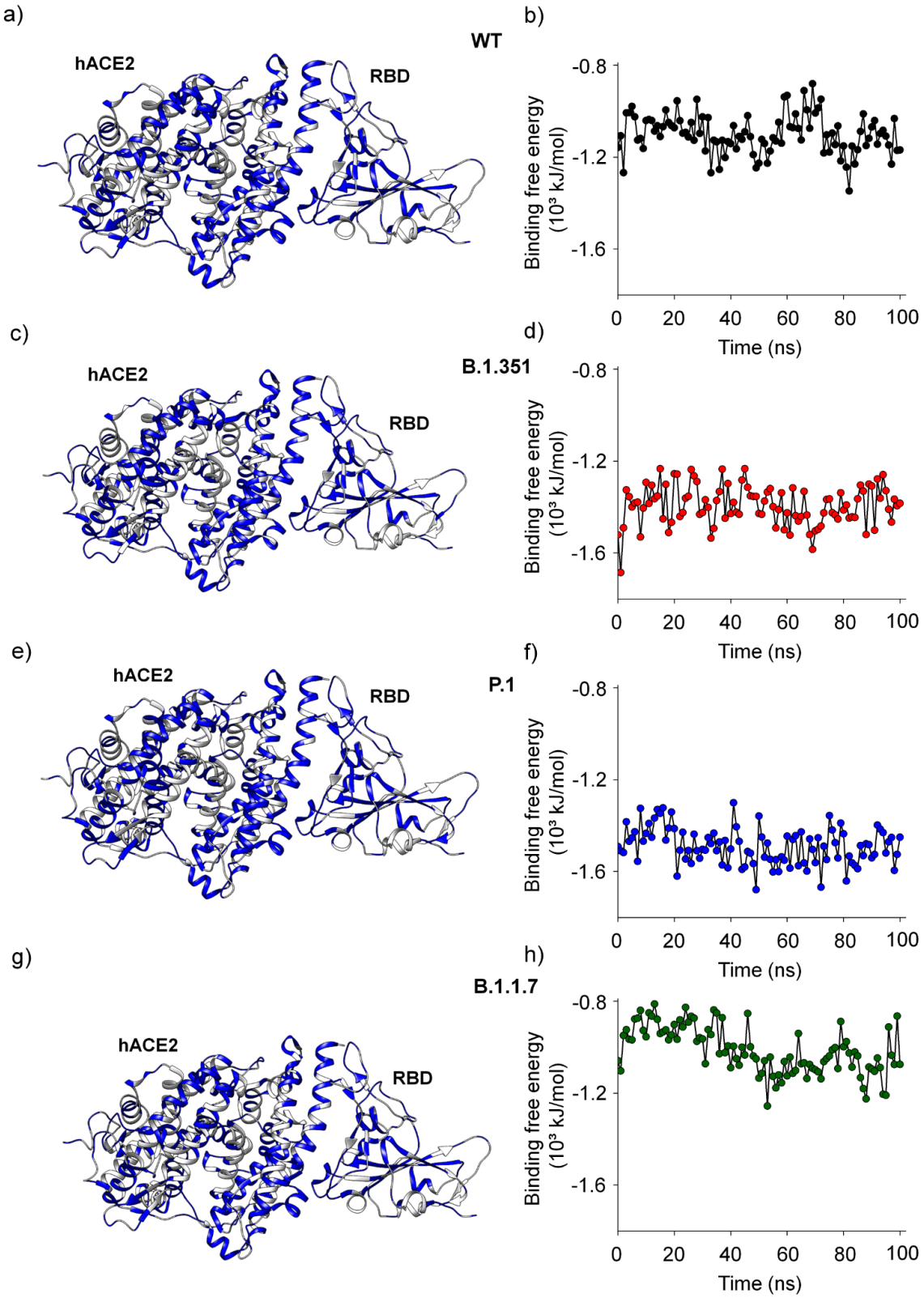

Figure S7. Binding free energies of RBD and its variants for formation of a complex with hACE2. Painels **b)**, **d)**, **f)** and **h)** show binding free energies as function of time using MD trajectories of the RBD^{WT} and its variants in complex with hACE2. Painels

a), **c)**, **e)** and **g)** show energy contributions of each residue for binding free energy, in which blue and white colors represent favorable and unfavorable contributions, respectively.

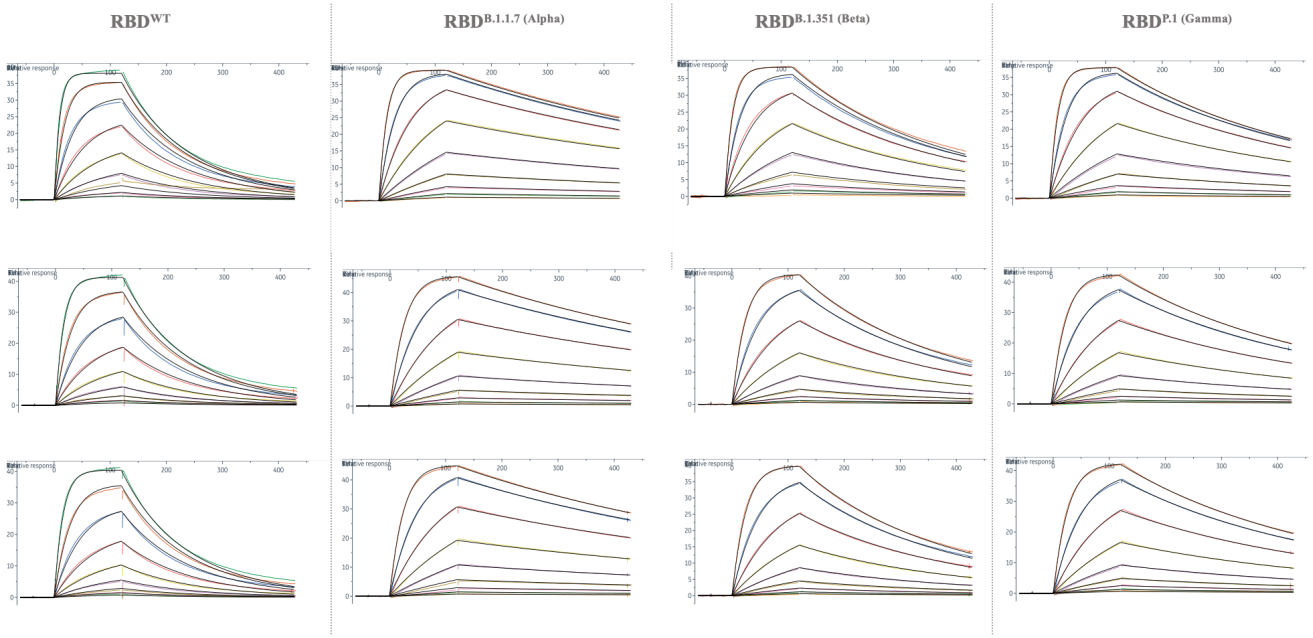

Figure S8. Surface plasmon resonance (SPR) sensorgrams using immobilized recombinant dimer hACE2 and different concentrations of purified recombinant Spike RBD and their variants, as described on materials and methods. The experimental data were fitted to a 1:1 binding model using Biacore Evaluation Software (GE Healthcare) to calculate the kinetics parameters (k_a and k_d) shown in **Table 1** and **Table S7**. At least eight different RBD concentrations were used to calculate the KD values.The results of the three biological replicates of the SPR assays are shown.

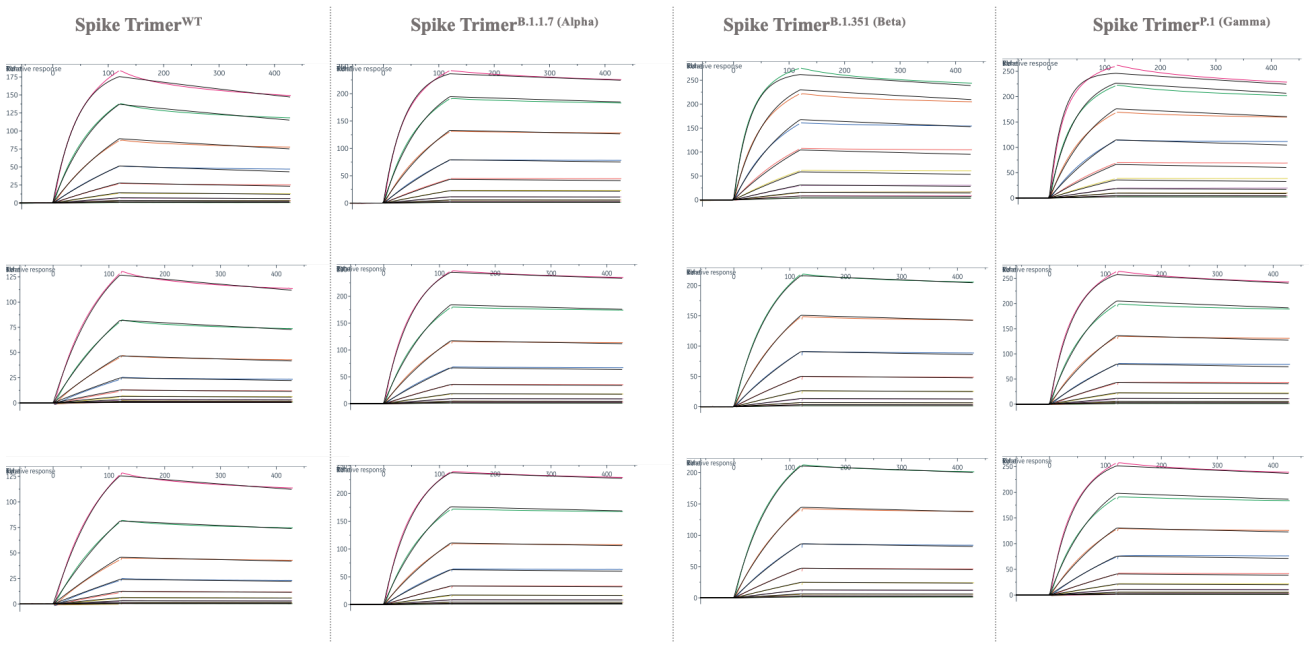

Figure S9. Surface plasmon resonance (SPR) sensorgrams using immobilized recombinant dimer hACE2 and different concentrations of purified recombinant Spike trimer and their variants, as described on materials and methods. The experimental data were fitted to a 1:1 binding model using Biacore Evaluation Software (GE Healthcare) to calculate the kinetics parameters (k_a and k_d) shown in **Table 1** and **Table S7**. At least seven different Spike concentrations were used to calculate the K_D values. The results of the three biological replicates of the SPR assays are shown.

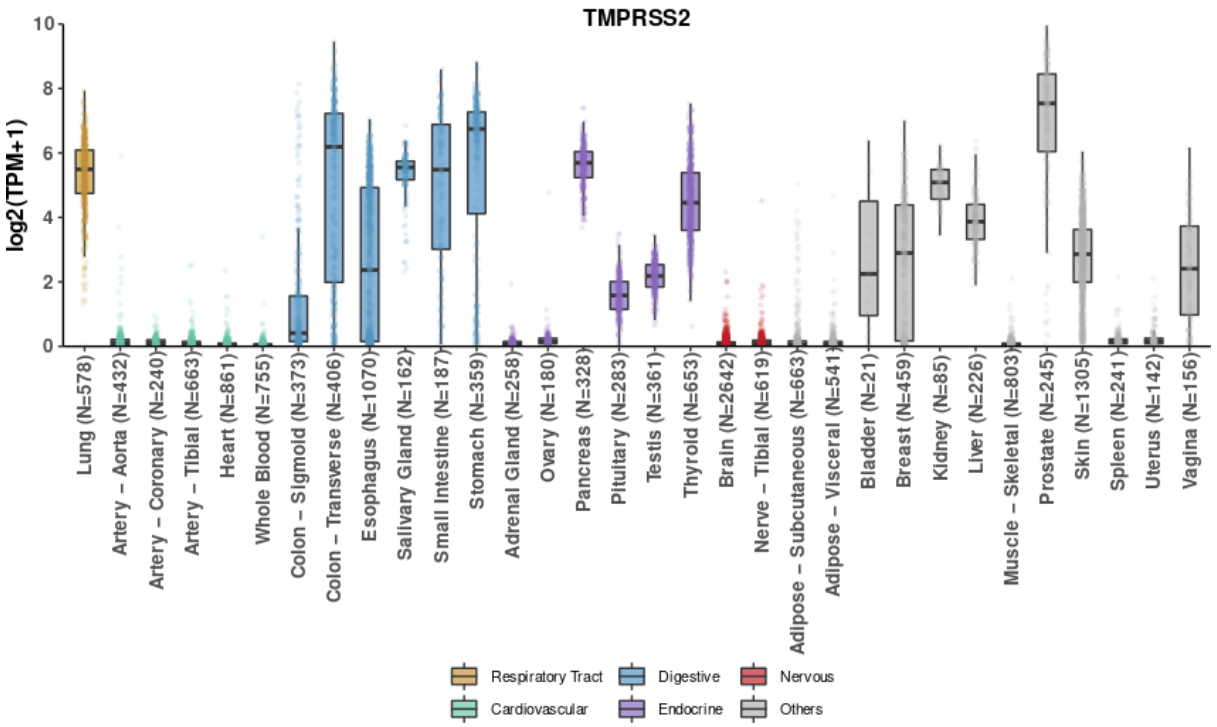

Figure S10. TMPRSS2 is mainly expressed in digestive, endocrine and few other human tissues or organs. Box colors represent different tissue groups according to their major functions. Numbers of samples are shown in parentheses.

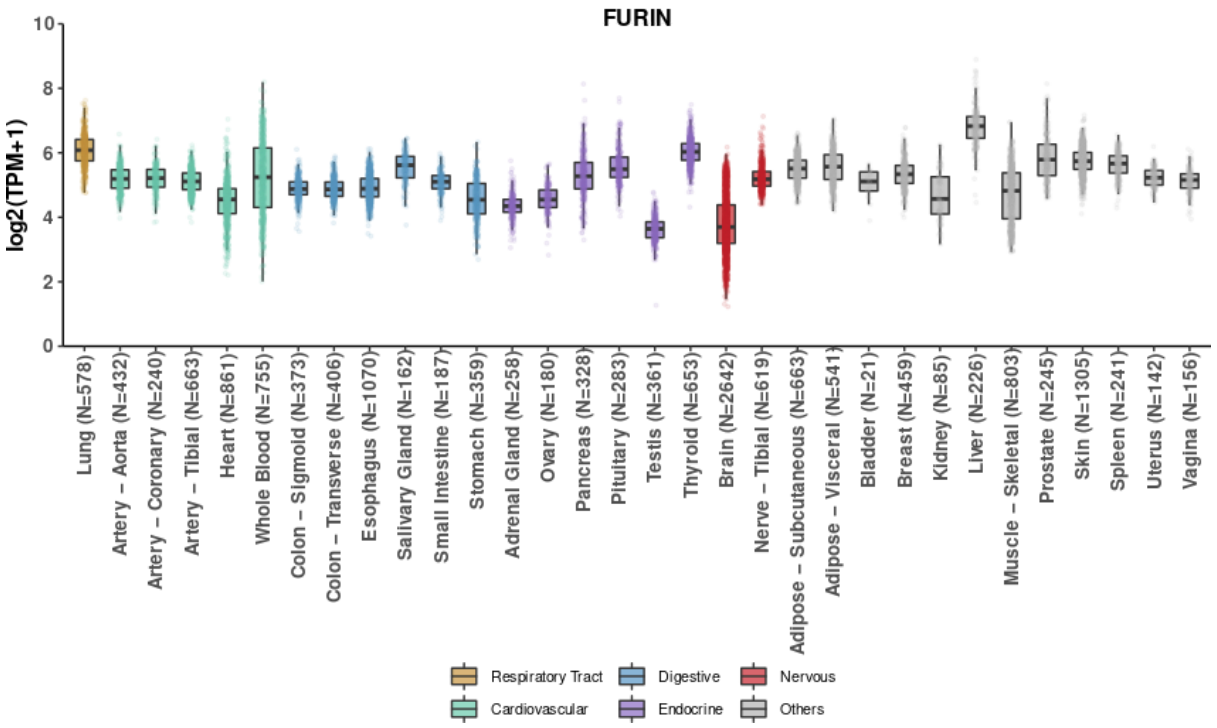

Figure S11. FURIN is highly expressed in all human tissues. Box colors represent different tissue groups according to their major functions. Numbers of samples are shown in parentheses.

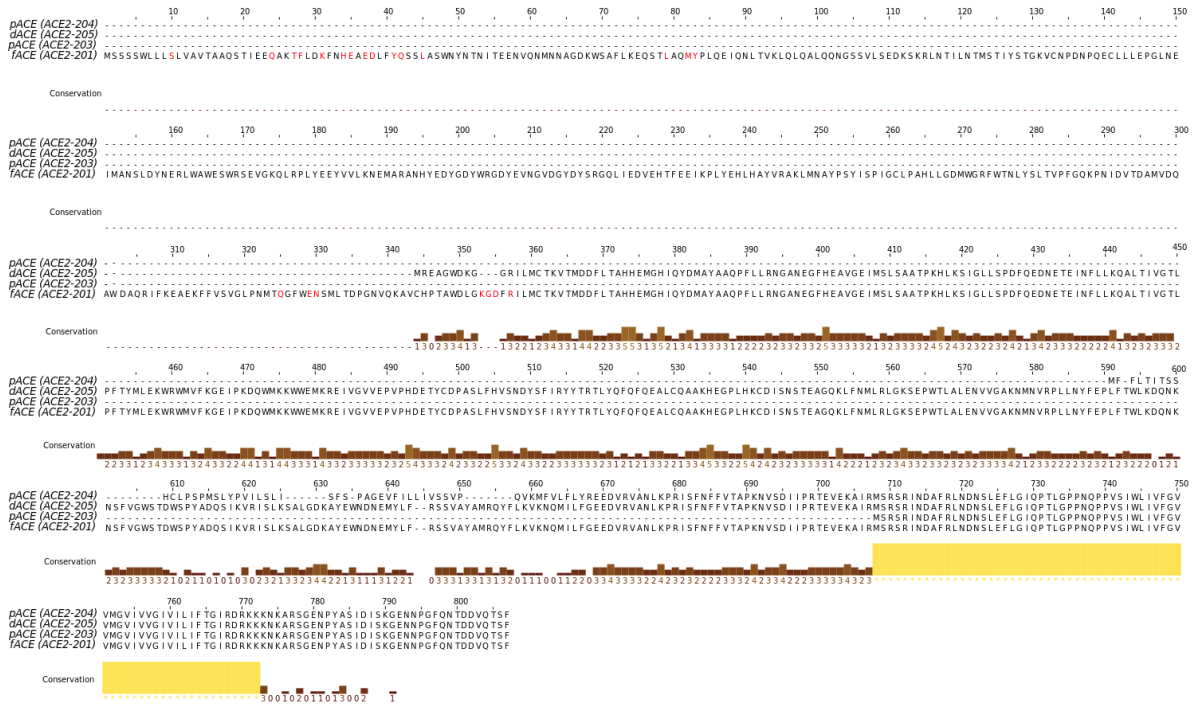

Figure S12. Multiple alignment of translated ACE2 transcripts. Transcripts were classified by fACE (full-length ACE), which is represented by the canonical isoform ACE2-201 and have all functional domains; dACE, that lacks RBD domain

interaction residues; and pACE, representing all other shorter ACE2 isoforms not neither reported in fACE or dACE classes. Residues marked in red correspond to direct contact portions of hACE2 with RBD domain.

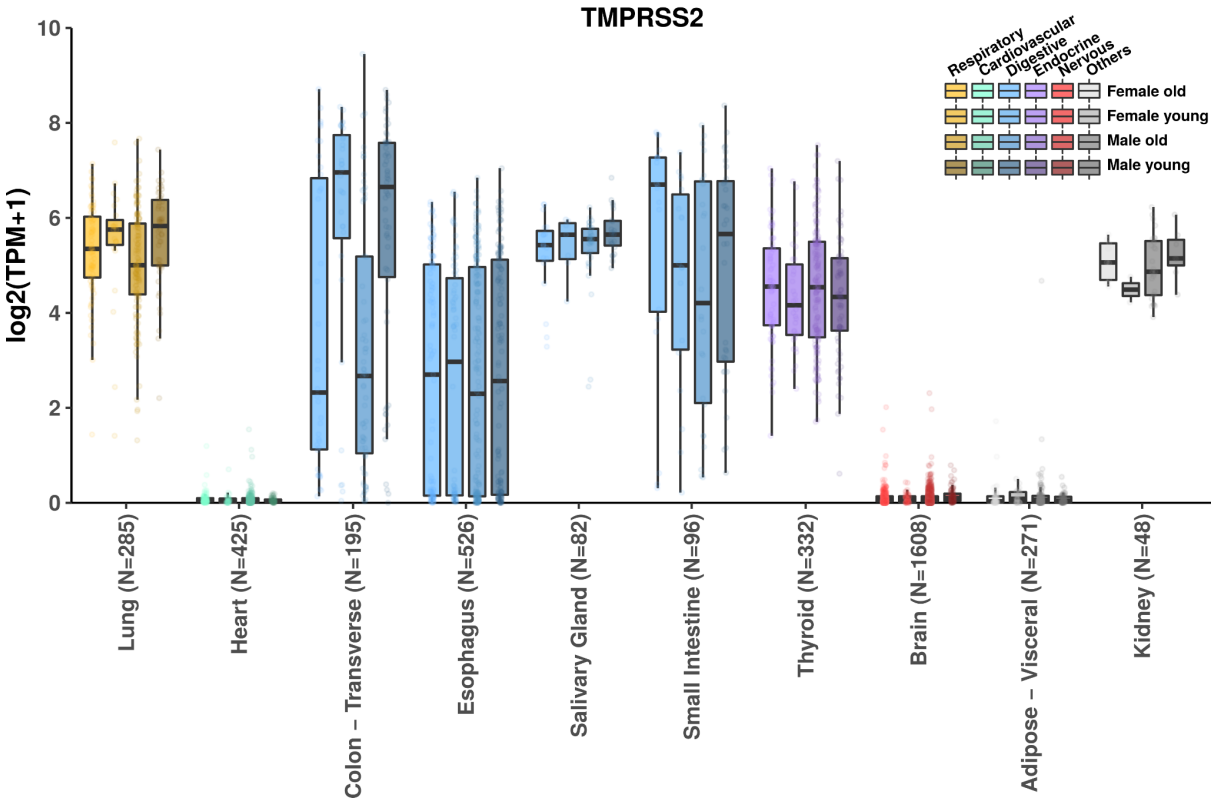

Figure S13. Tissue-wide TMPRSS2 expression by age and gender. Box colors represent different tissue groups according to their major functions. Box shades refer to distinct clinical variables, either age (lighter) or gender (darker).

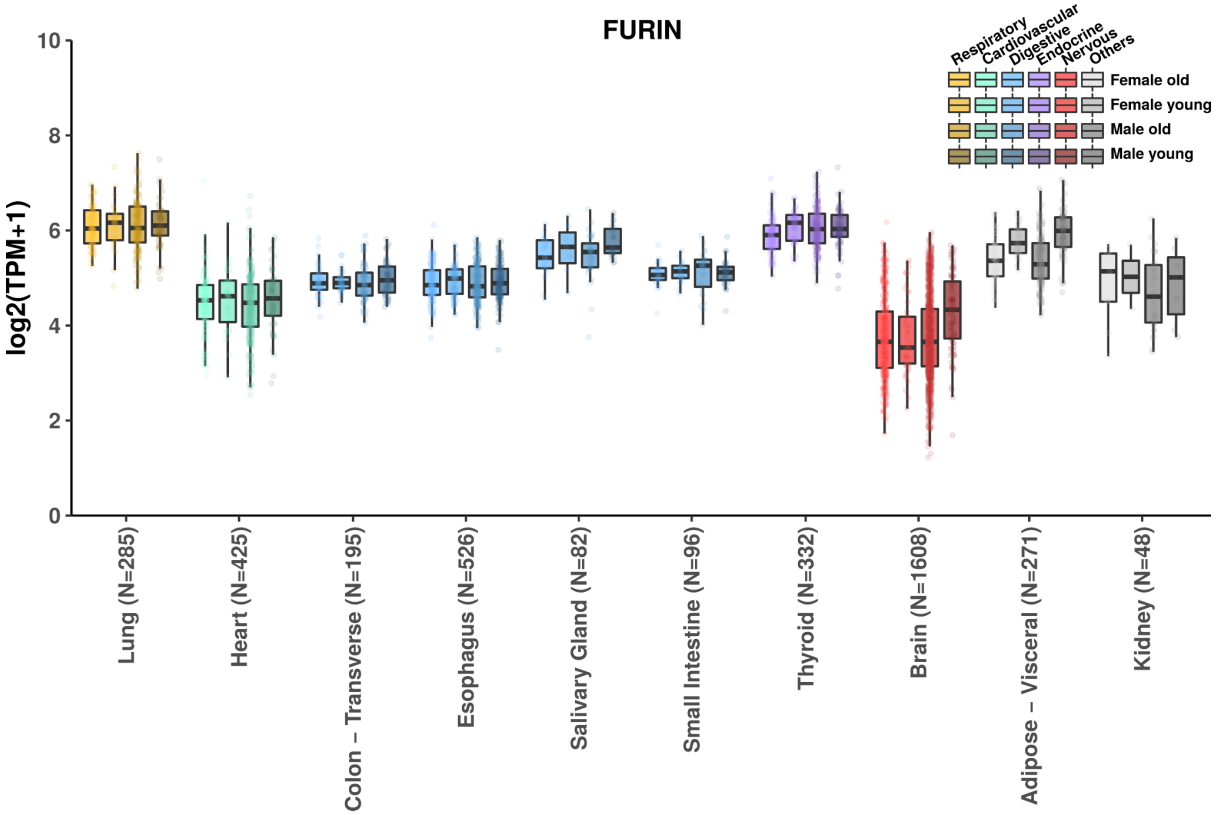

Figure S14. Tissue-wide FURIN expression by age and gender. Box colors represent different tissue groups according to their major functions. Box shades refer to distinct clinical variables, either age (lighter) or gender (darker).

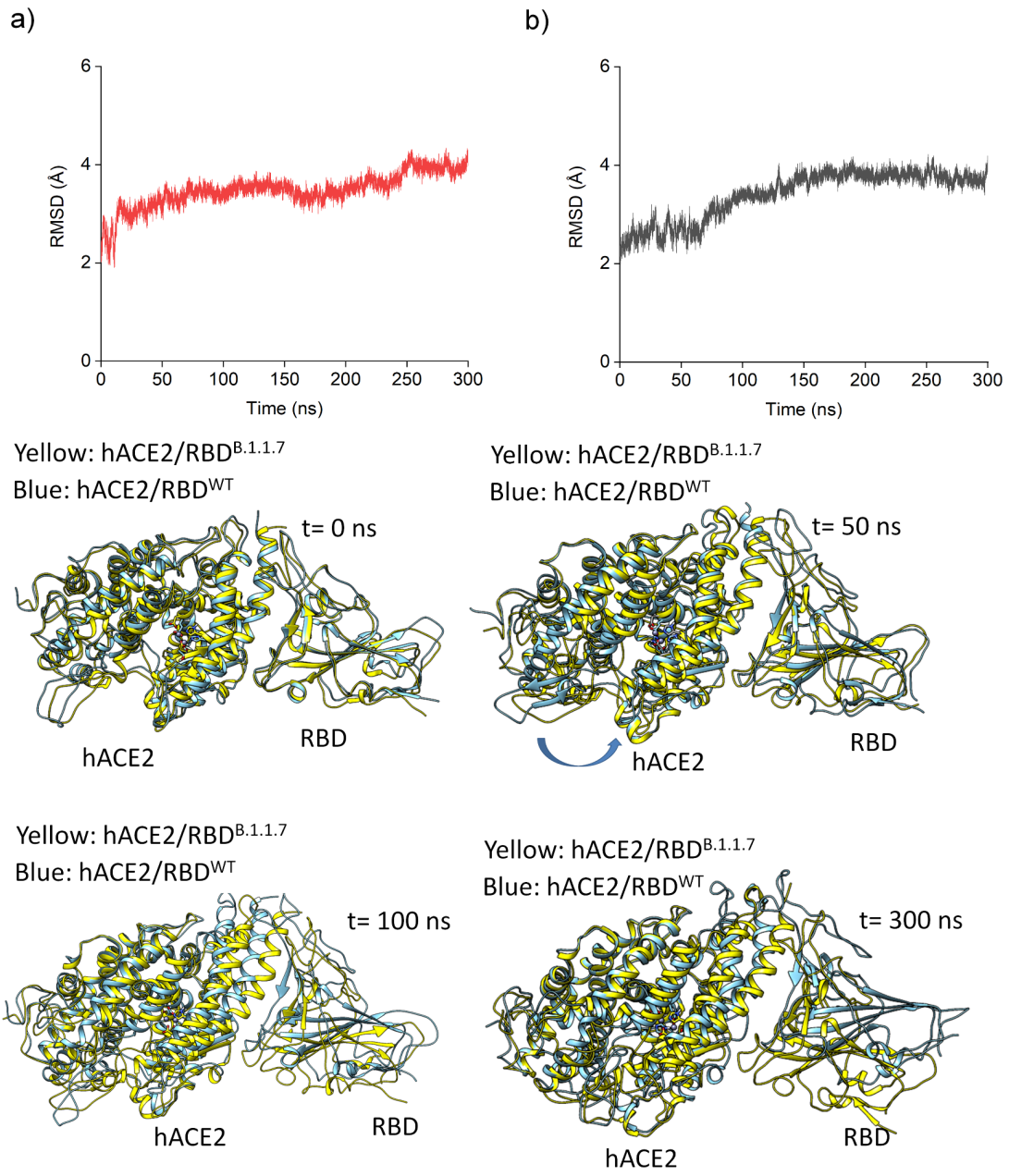

Figure S15. Illustration about conformational changes of hACE2. a) Backbone RMSD of hACE2 in complex with RBD^{WT}. **b)** Backbone RMSD of hACE2 in complex with RBD^{Alpha}. Structural superposition of the complexes in times 0, 50, 100 and 300 ns. It is observed that the hACE2 enzymatic cavity closes faster when it interacts with RBD^{Alpha} than RBD^{WT}, as observed at 50 ns (blue arrow).

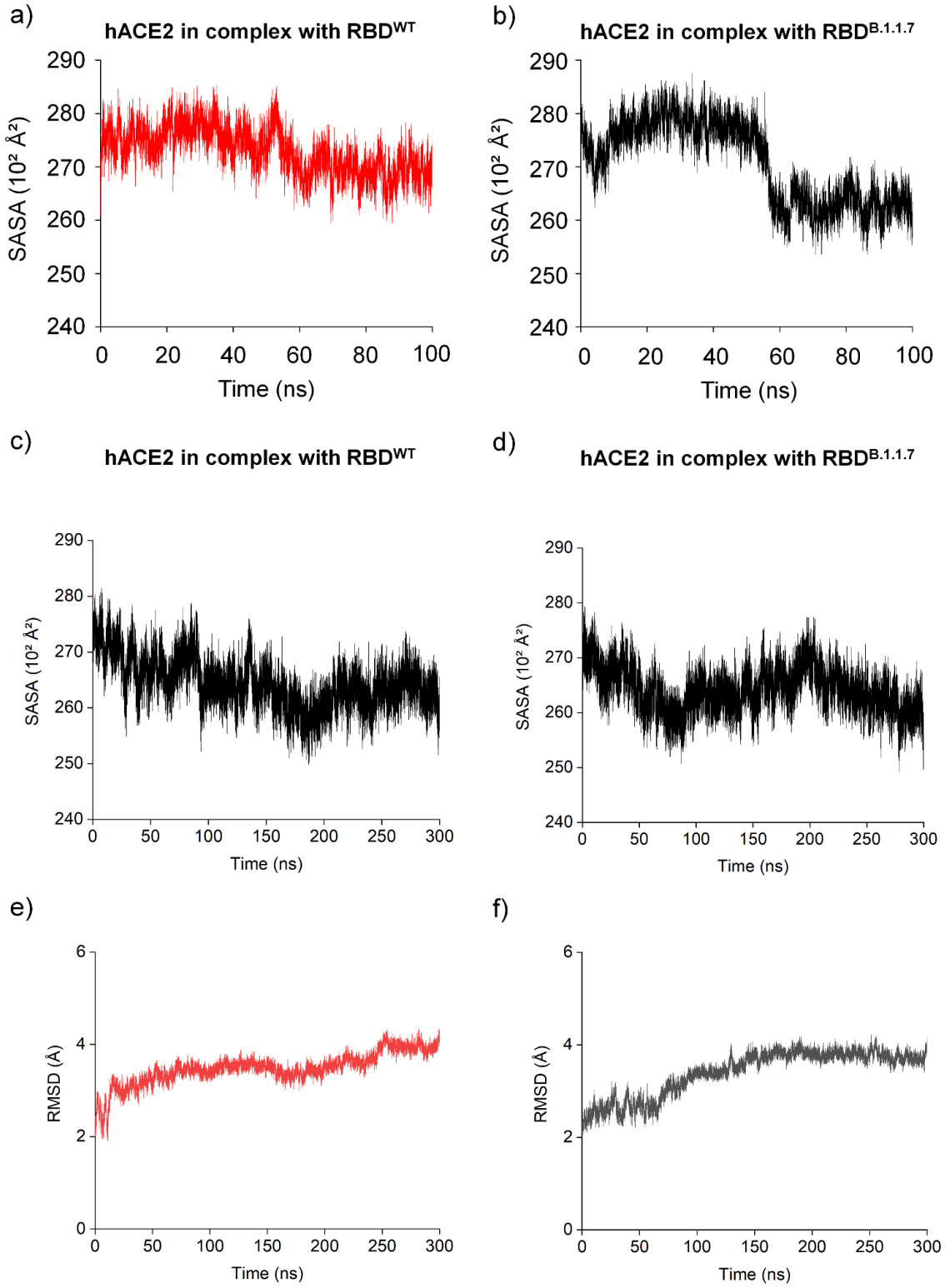

Figure S16. Conformational changes of hACE2 while interacting with RBD of the Alpha variant and wild type. a) Simulation 1 for 100 ns showing SASA values of hACE2 in complex with RBD^{WT}. **b)** Simulation 1 for 100 ns showing SASA values of hACE2 in complex with $RBD^{B.1.1.7}$. The panels **c)** and **e)** are results of the independent calculation (300 ns), comparing backbone RMSD of the hACE2 in

complex with RBD^{WT}. The panels **d)** and **f)** are results of the independent calculation (300 ns), comparing backbone RMSD of the hACE2 in complex with $RBD^{B.1.1.7}$. These results were similar to 100 ns, showing that RMSD and SASA values converged after 50 ns, in agreement with the second simulation (300 ns).

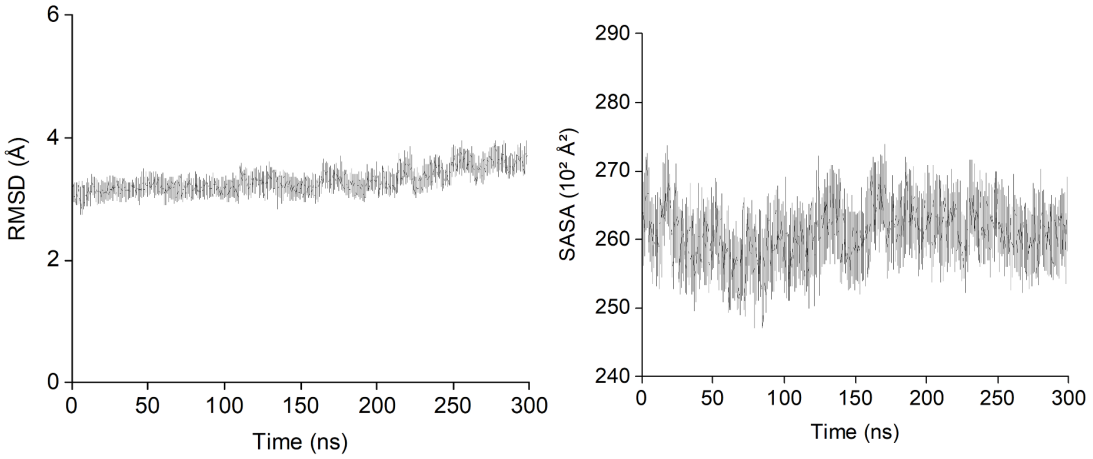

Figure S17. Conformational changes of hACE2, in complex with $RBD^{P.1}$, and their relationships with SASA values.

Table S1.

Insights about SARS-CoV-2 variants. Insights about origin, mutations and number of countries relating cases associated with each variant. NA, not available.

SARS-CoV-2 Variant	Country First Detected	Number of countries that reported the variant (25 May 2021)	Spike Protein mutations
B.1.1.7[19] (Alpha)	United Kingdom, London	149[20]	Deletion 69/70 Deletion 144/145 N501Y A570D D614G P681H T716I S982A D1118H
B.1.351[21] (Beta)	South Africa	102[20]	L18F D80A D215G Deletion 242/244 R246I K417N E484K N501Y D614G A701V
P.1[22] (Gamma)	Brazil, Manaus	59[20]	L18F T20N P26S D138Y R190S K417T E484K N501Y D614G H655Y T1027I V1176F
B.1.617.2[23] (Delta)	India	54[20]	T19R Deletion 157/158 L452R T478K D614G P681R D950N
B.1.427/429[24,25] (Epsilon)	United States, California	29 (01 Abril 2021)[26]	S13I W152C

			L452R D614G
B.1.526[27] (Iota)	United States, New York	NA	L5F T95I D253G E484K D614G A701V
B.1.617.1[28] (kappa)	India	41[20]	L452R E484Q D614G P681R Q1071H

Table S2. Insights about SARS-CoV-2 variants. Compared with wild-type, variants presented significant increases of transmissibility, symptoms, time of infectivity, viral load, severity, lethality, binding affinity and replication rate. ND: undetermined information; NA: unavailable information.

	B.1.1.7	**P.1**	**B.1.351**	**B.1.429/427**
Increase of transmissibility	10 - 75% [29],[30],[31],[32],[33],[34],[35],[36],[37]	12 - 46% [29],[38],[36]	55%[36],[37]	6-24%[39],[32]
Higher viral load	20 - 30% [40],[41,42],16,17,[43],[36]	10 fold [44],[36]	ND [41],[36]	2 fold [39]
More severe disease	40-65%[37],[45],[46]	ND[46]	ND[46]	NA
Higher lethality	8 - 71% [47],[31],[48],[49],[50],[37],[45]	ND [46]	ND [46],[51]	NA
More binding affinity to ACE2 in relation to RBD^{WT}	~2 fold[52]	NA	~4.6 fold[52]	NA

Table S3. Hydrogen bonding occupancy (%) of interactions between RBD of SARS-CoV-2 variants and hACE2. Hydrogen bond occupancy (%) analysis of the RBD residues and its variants that make contact with hACE2 along different MD trajectories. Table shows intramolecular and intermolecular interactions in hACE2 and RBD. Cut-off: hydrogen bond distance of 3 Å between hydrogen and nitrogen or oxygen. sc = side chain and mc = main chain.

HB donor	HB acceptor	WT	B.1.351	P.1	B.1.1.7
R482-sc^{RBD}	E489-sc^{RBD}			90.7	87.7
N487-sc^{RBD}	A475-mc^{hACE2}				15.8
Q493-sc^{RBD}	E35-sc^{hACE2}	51.9	40.4	42.8	4.4
Q498-sc^{RBD}	D38-sc^{hACE2}	38.7		14.6	
E489-mc^{RBD}	E489-sc^{RBD}	50.0	54.9	33.5	50.1
K31-sc^{hACE2}	Q493-sc^{RBD}	19.6	9.0	16.7	
K475-sc^{RBD}	E495-sc^{RBD}	23.4			
T449-sc^{RBD}	R273-mc^{hACE2}	26.9	41.3	57.3	27.9
T453-sc^{RBD}	T449-mc^{RBD}	44.2		41.0	
T500-scRBD	Y41-sc^{hACE2}	35.8	10.3	13.7	
T500-sc^{RBD}	D355-sc^{hACE2}	1.7		19.0	
T500-sc^{RBD}	G354-mc^{hACE2}				33.1
Y449-sc^{RBD}	D38-sc^{hACE2}	63.2	59.2	56.7	4.7
T453-sc^{RBD}	T449-mc^{RBD}		33.7		45.8
K484-sc^{RBD}	E75-sc^{hACE2}		1.5	1.2	
F490-mc^{RBD}	E484-sc^{RBD}	0.1			66.5
G485-mc^{RBD}	E484-sc^{RBD}	17.0			
K31-sc^{hACE2}	E484-sc^{RBD}	~0.0			47.4
F486-mc^{RBD}	E484-sc^{RBD}	19.0			
Y489-sc^{RBD}	N487-sc^{RBD}	15.4			
Y489-sc^{RBD}	Y83-sc^{hACE2}	4.1		22.5	
Y495-sc^{RBD}	E406-sc^{hACE2}	59.2	26.5	15.5	28.9
K417-sc^{RBD}	D30-sc^{hACE2}	51.5			28.2
K417-sc^{RBD}	H34-sc^{hACE2}	13.5			8.2
K417-sc^{RBD}	L455-mc^{RBD}	5.4			
Y501-sc^{RBD}	G496-mc^{RBD}		21.3	13.9	1.7
Y501-sc^{RBD}	Q498-sc^{RBD}			25.9	
Y501-sc^{RBD}	K353-mc^{hACE2}				18.7
Y501-sc^{RBD}	Y41-sc^{hACE2}				2.8

Table S4. Count of positive and negative correlations using cross-correlation analysis. correlation analysis of MD trajectories of RBD variants and WT OF SARS-CoV-2. Total correlation pairs observed in the interaction of RBD^{WT} and its variants with hACE2.

	Correlation	Intra-RBD	Inter	Intra-ACE2
WT	positive	25488	50848	161492
	negative	11954	64970	194320
B.1.351	positive	7300	67747	190816
	negative	30142	48071	164996
P.1	positive	30200	51365	166086
	negative	7242	64453	189726
B.1.1.7	positive	24822	46852	176502
	negative	12620	58220	179310

Table S5. Count of relevant positive and negative correlations using cross-correlation analysis. Pairs of C_α exhibiting correlation higher than 0.8 were analyzed in the interaction of RBD^{WT} and its variants while interacting with hACE2.

	Correlation	Intra-RBD	Inter	Intra-ACE2
WT	positive	436	21	3088
	negative	0	0	0
B.1.351	positive	466	8	3656
	negative	0	0	0
P.1	positive	458	135	4160
	negative	0	1	0
B.1.1.7	positive	924	384	6852
	negative	0	0	76

Table S6. Binding enthalpy/energy between RBD of different SARS-CoV-2 variants and hACE2. The entropy is not included for binding free energy calculation [12].

	Energy (kJ/mol)				
Variants	**vdW**	**Coul**	**Polar**	**SASA**	**ΔG**
B.1.351	-368 ± 33	-1453 ± 80	472 ± 85	-44 ± 4	-1393 ± 84
P.1	-430 ± 52	-1461 ± 79	454 ± 85	-52 ± 6	-1489 ± 78
B.1.1.7	-297 ± 32	-1285 ± 76	612 ± 147	-42 ± 6	-1013 ± 101
WT	-352 ± 341	-1380 ± 86	678 ± 87	-46 ± 4	-1100 ± 85

Table S7. Kinetic parameters obtained from surface plasmon resonance (SPR) assays. More details on material and methods.

Variant	Capture Level (RU)	Spike Protein Concentrations (nM)	k_a (10^6 $M^{-1}s^{-1}$)	k_d (10^{-4} s^{-1})	K_D (nM)	R_{max} (RU)	Chi^2 (RU^2)
RBD^{WT}	176.1	0.488 - 125	6.6 ± 2.0	93.4 ± 1.7	15.0 ± 4.1	44.7 ± 3.1	0.35 ± 0.23
$RBD^{B.1.1.7(Alpha)}$	174.1	0.244 - 62.5	9.0 ± 3.0	15.5 ± 0.1	1.8 ± 0.5	44.6 ± 4.0	0.05 ± 0.01
$RBD^{B.1.351(Beta)}$	173.3	0.244 - 62.5	9.0 ± 2.7	40.9 ± 1.3	4.8 ± 1.4	42.6 ± 2.0	0.9 ±0.07
$RBD^{P.1(Gamma)}$	170.5	0.244 - 62.5	9.0 ± 3.4	27.8 ± 0.9	3.3 ± 1.0	43.1 ± 3.5	0.05 ± 0.01
Spike $trimer^{WT}$	169.4	0.488 - 250	0.7 ± 0.2	4.8 ± 0.8	6.7 ± 1.3	174.1 ± 17.6	0.81 ± 0.62
Spike $trimer^{B.1.1.7(Alpha)}$	174.5	0.488 - 250	0.8 ± 0.2	1.5 ± 0.1	1.9 ± 0.2	265.0 ± 14.2	1.93 ± 0.39
Spike $trimer^{B.1.351(Beta)}$	178.4	0.488 - 125	1.6 ± 0.9	2.1 ± 0.7	1.4 ± 0.3	268.0 ± 0.9	5.70 ± 8.90
Spike $trimer^{P.1(Gamma)}$	170.5	0.488 - 250	1.2 ± 0.5	2.4 ± 0.5	2.1 ± 0.3	266.5 ± 15.1	7.92 ± 6.32

Table S8. Experimental K_D obtained by different kinetic assays. ND: not determined.

Experimental assay	Construction	$K_D^{B.1.351}$ (nM)	$K_D^{B.1.1.7}$ (nM)	$K_D^{P.1}$ (nM)	K_D^{WT} (nM)
Microscale thermophoresis[52]	RBD	87.6	203.7	ND	402.5
bio-layer interferometry[53]	RBD	ND	22	ND	133
SPR[54]	RBD	48.2	13.1	ND	56.9
SPR[55]	RBD	4.8	9.1	ND	14
bio-layer interferometry[56]	Spike trimer	3.2-13.7	0.1-2.4	ND	ND
SPR[57–59]	RBD	ND	ND	ND	5.1 - 44.2

Table S9. Eigenvalues of the principal components 1 and 2, PC1 and PC2 respectively, obtained from diagonalizations of the 7119x7119 correlation matrix (representing backbone hACE2) and 5373x5373 correlation matrix (representing backbone RBD).

SARS-CoV-2/hACE2	Protein	Eigenvalue (PC1)	Eigenvalue (PC2)
WT	hACE2	12.9	6.4
	RBD^{WT}	1.7	0.9
B.1.1.7 (Alpha)	hACE2	32.5	4.0
	$RBD^{B.1.1.7(Alpha)}$	2.3	1.0
B.1.351 (Beta)	hACE2	9.5	5.8
	$RBD^{B.1.351(Beta)}$	1.3	1.0
P.1 (Gamma)	hACE2	20.3	3.3
	$RBD^{P.1(Gamma)}$	4.6	2.1

REFERENCES

1. Lan J, Ge J, Yu J, Shan S, Zhou H, Fan S, et al. Structure of the SARS-CoV-2 spike receptor-binding domain bound to the ACE2 receptor. Nature. 2020;581: 215–220. doi:10.1038/s41586-020-2180-5

2. Pettersen EF, Goddard TD, Huang CC, Couch GS, Greenblatt DM, Meng EC, et al. UCSF Chimera--a visualization system for exploratory research and analysis. J Comput Chem. 2004;25: 1605–1612. doi:10.1002/jcc.20084

3. Maestro | Schrödinger. [cited 15 Jun 2020]. Available: https://www.schrodinger.com/maestro

4. Rostkowski M, Olsson MHM, Søndergaard CR, Jensen JH. Graphical analysis of pH-dependent properties of proteins predicted using PROPKA. BMC Struct Biol. 2011;11: 6. doi:10.1186/1472-6807-11-6

5. Pronk S, Páll S, Schulz R, Larsson P, Bjelkmar P, Apostolov R, et al. GROMACS 4.5: a high-throughput and highly parallel open source molecular simulation toolkit. Bioinformatics. 2013;29: 845–854. doi:10.1093/bioinformatics/btt055

6. Van Der Spoel D, Lindahl E, Hess B, Groenhof G, Mark AE, Berendsen HJC. GROMACS: fast, flexible, and free. J Comput Chem. 2005;26: 1701–1718. doi:10.1002/jcc.20291

7. Lindahl E, Hess B, van der Spoel D. GROMACS 3.0: a package for molecular simulation and trajectory analysis. Journal of Molecular Modeling. 2001. pp. 306–317. doi:10.1007/s008940100045

8. Abraham MJ, Murtola T, Schulz R, Páll S, Smith JC, Hess B, et al. GROMACS: High performance molecular simulations through multi-level parallelism from laptops to supercomputers. SoftwareX. 2015. pp. 19–25. doi:10.1016/j.softx.2015.06.001

9. Robertson MJ, Tirado-Rives J, Jorgensen WL. Improved Peptide and Protein Torsional Energetics with the OPLSAA Force Field. J Chem Theory Comput. 2015;11: 3499–3509. doi:10.1021/acs.jctc.5b00356

10. Zoete V, Cuendet MA, Grosdidier A, Michielin O. SwissParam: a fast force field generation tool for small organic molecules. J Comput Chem. 2011;32: 2359–2368. doi:10.1002/jcc.21816

11. Grant BJ, Rodrigues APC, ElSawy KM, McCammon JA, Caves LSD. Bio3d: an R package for the comparative analysis of protein structures. Bioinformatics. 2006. pp. 2695–2696. doi:10.1093/bioinformatics/btl461

12. Kumari R, Kumar R, Open Source Drug Discovery Consortium, Lynn A. g_mmpbsa--a GROMACS tool for high-throughput MM-PBSA calculations. J Chem Inf Model. 2014;54: 1951–1962. doi:10.1021/ci500020m

13. Bray NL, Pimentel H, Melsted P, Pachter L. Near-optimal probabilistic RNA-seq quantification. Nat Biotechnol. 2016;34: 525–527. doi:10.1038/nbt.3519

14. Larkin MA, Blackshields G, Brown NP, Chenna R, McGettigan PA, McWilliam H, et al. Clustal W and Clustal X version 2.0. Bioinformatics. 2007;23: 2947–2948.

doi:10.1093/bioinformatics/btm404

15. Rombel IT, Sykes KF, Rayner S, Johnston SA. ORF-FINDER: a vector for high-throughput gene identification. Gene. 2002;282: 33–41. doi:10.1016/s0378-1119(01)00819-8

16. Celik I, Yadav R, Duzgun Z, Albogami S, El-Shehawi AM, Fatimawali, et al. Interactions of the Receptor Binding Domain of SARS-CoV-2 Variants with hACE2: Insights from Molecular Docking Analysis and Molecular Dynamic Simulation. Biology . 2021;10. doi:10.3390/biology10090880

17. Celik I, Khan A, Dwivany FM, Fatimawali, Wei D-Q, Tallei TE. Computational prediction of the effect of mutations in the receptor-binding domain on the interaction between SARS-CoV-2 and human ACE2. Mol Divers. 2022. doi:10.1007/s11030-022-10392-x

18. Zhu X, Mannar D, Srivastava SS, Berezuk AM, Demers J-P, Saville JW, et al. Cryo-electron microscopy structures of the N501Y SARS-CoV-2 spike protein in complex with ACE2 and 2 potent neutralizing antibodies. PLoS Biol. 2021;19: e3001237. doi:10.1371/journal.pbio.3001237

19. Alaa Abdel Latif, Julia L. Mullen, Manar Alkuzweny, Ginger Tsueng, Marco Cano, Emily Haag, Jerry Zhou, Mark Zeller, Nate Matteson, Chunlei Wu, Kristian G. Andersen, Andrew I. Su, Karthik Gangavarapu, Laura D. Hughes, and the Center for Viral Systems Biology. B.1.1.7 Lineage Report. In: Outbreak.info [Internet]. [cited 14 May 2021]. Available: https://outbreak.info/situation-reports?pango=B.1.1.7&loc=GBR&loc=USA&loc=USA_US-CA&selected=GBR

20. Weekly epidemiological update on COVID-19 - 25 May 2021. [cited 26 May 2021]. Available: https://www.who.int/publications/m/item/weekly-epidemiological-update-on-covid-19---25-may-2021

21. Ho D, Wang P, Liu L, Iketani S, Luo Y, Guo Y, et al. Increased Resistance of SARS-CoV-2 Variants B.1.351 and B.1.1.7 to Antibody Neutralization. doi:10.21203/rs.3.rs-155394/v1

22. Alaa Abdel Latif, Julia L. Mullen, Manar Alkuzweny, Ginger Tsueng, Marco Cano, Emily Haag, Jerry Zhou, Mark Zeller, Nate Matteson, Chunlei Wu, Kristian G. Andersen, Andrew I. Su, Karthik Gangavarapu, Laura D. Hughes, and the Center for Viral Systems Biology. P.1 Lineage Report. In: Outbreak.info [Internet]. [cited 14 May 2021]. Available: https://outbreak.info/situation-reports?pango=P.1&selected=BRA&loc=BRA&loc=USA&loc=USA_US-CA

23. Alaa Abdel Latif, Julia L. Mullen, Manar Alkuzweny, Ginger Tsueng, Marco Cano, Emily Haag, Jerry Zhou, Mark Zeller, Nate Matteson, Chunlei Wu, Kristian G. Andersen, Andrew I. Su, Karthik Gangavarapu, Laura D. Hughes, and the Center for Viral Systems Biology. B.1.617.2 Lineage Report. In: Outbreak.info [Internet]. [cited 14 May 2021]. Available: https://outbreak.info/situation-reports?pango=B.1.617.2&loc=IND&loc=GBR&loc=USA&selected=IND

24. Alaa Abdel Latif, Julia L. Mullen, Manar Alkuzweny, Ginger Tsueng, Marco Cano, Emily Haag, Jerry Zhou, Mark Zeller, Nate Matteson, Chunlei Wu, Kristian G. Andersen,

Andrew I. Su, Karthik Gangavarapu, Laura D. Hughes, and the Center for Viral Systems Biology. B.1.427 Lineage Report. In: Outbreak.info [Internet]. [cited 14 May 2021]. Available: https://outbreak.info/situation-reports?pango=B.1.427&loc=USA&loc=USA_US-CA&selected=USA_US-CA

25. Alaa Abdel Latif, Julia L. Mullen, Manar Alkuzweny, Ginger Tsueng, Marco Cano, Emily Haag, Jerry Zhou, Mark Zeller, Nate Matteson, Chunlei Wu, Kristian G. Andersen, Andrew I. Su, Karthik Gangavarapu, Laura D. Hughes, and the Center for Viral Systems Biology. B.1.429 Lineage Report. In: Outbreak.info [Internet]. [cited 14 May 2021]. Available: https://outbreak.info/situation-reports?pango=B.1.429&loc=USA&loc=USA_US-CA&selected=USA_US-CA

26. McCallum M, Bassi J, De Marco A, Chen A, Walls AC, Di Iulio J, et al. SARS-CoV-2 immune evasion by variant B.1.427/B.1.429. bioRxiv. 2021. p. 2021.03.31.437925. doi:10.1101/2021.03.31.437925

27. Alaa Abdel Latif, Julia L. Mullen, Manar Alkuzweny, Ginger Tsueng, Marco Cano, Emily Haag, Jerry Zhou, Mark Zeller, Nate Matteson, Chunlei Wu, Kristian G. Andersen, Andrew I. Su, Karthik Gangavarapu, Laura D. Hughes, and the Center for Viral Systems Biology. B.1.526 Lineage Report. In: Outbreak.info [Internet]. [cited 14 May 2021]. Available: https://outbreak.info/situation-reports?pango=B.1.526&loc=USA&loc=USA_US-NY&selected=USA_US-NY

28. Alaa Abdel Latif, Julia L. Mullen, Manar Alkuzweny, Ginger Tsueng, Marco Cano, Emily Haag, Jerry Zhou, Mark Zeller, Nate Matteson, Chunlei Wu, Kristian G. Andersen, Andrew I. Su, Karthik Gangavarapu, Laura D. Hughes, and the Center for Viral Systems Biology. B.1.617.1 Lineage Report. In: Outbreak.info [Internet]. [cited 14 May 2021]. Available: https://outbreak.info/situation-reports?pango=B.1.617.1&loc=IND&loc=GBR&loc=USA&selected=IND

29. Stefanelli P, Trentini F, Guzzetta G, Marziano V, Mammone A, Poletti P, et al. Co-circulation of SARS-CoV-2 variants B.1.1.7 and P.1. medRxiv. 2021; 2021.04.06.21254923. doi:10.1101/2021.04.06.21254923

30. Lee LYW, Rozmanowski S, Pang M, Charlett A, Anderson C, Hughes GJ, et al. SARS-CoV-2 infectivity by viral load, S gene variants and demographic factors and the utility of lateral flow devices to prevent transmission. medRxiv. 2021; 2021.03.31.21254687. doi:10.1101/2021.03.31.21254687

31. Davies NG, Jarvis CI, CMMID COVID-19 Working Group, Edmunds WJ, Jewell NP, Diaz-Ordaz K, et al. Increased mortality in community-tested cases of SARS-CoV-2 lineage B.1.1.7. Nature. 2021;593: 270–274. doi:10.1038/s41586-021-03426-1

32. Graham MS, Sudre CH, May A, Antonelli M, Murray B, Varsavsky T, et al. Changes in symptomatology, re-infection and transmissibility associated with SARS-CoV-2 variant B.1.1.7: an ecological study. medRxiv. 2021; 2021.01.28.21250680. doi:10.1101/2021.01.28.21250680

33. Davies NG, Abbott S, Barnard RC, Jarvis CI, Kucharski AJ, Munday JD, et al. Estimated transmissibility and impact of SARS-CoV-2 lineage B.1.1.7 in England. Science.

2021;372. doi:10.1126/science.abg3055

34. Volz E, Mishra S, Chand M, Barrett JC, Johnson R, Geidelberg L, et al. Transmission of SARS-CoV-2 Lineage B.1.1.7 in England: Insights from linking epidemiological and genetic data. doi:10.1101/2020.12.30.20249034

35. Munitz A, Yechezkel M, Dickstein Y, Yamin D, Gerlic M. BNT162b2 vaccination effectively prevents the rapid rise of SARS-CoV-2 variant B.1.1.7 in high-risk populations in Israel. Cell Rep Med. 2021;2: 100264. doi:10.1016/j.xcrm.2021.100264

36. Curran J, Dol J, Boulos L, Somerville M, McCulloch H, MacDonald M, et al. Transmission characteristics of SARS-CoV-2 variants of concern Rapid Scoping Review. doi:10.1101/2021.04.23.21255515

37. Risk assessment: SARS-CoV-2 - increased circulation of variants of concern and vaccine rollout in the EU/EEA, 14th update. 15 Feb 2021 [cited 21 May 2021]. Available: https://www.ecdc.europa.eu/en/publications-data/covid-19-risk-assessment-variants-vaccine-fourteenth-update-february-2021

38. Faria NR, Mellan TA, Whittaker C, Claro IM, Candido D da S, Mishra S, et al. Genomics and epidemiology of a novel SARS-CoV-2 lineage in Manaus, Brazil. medRxiv. 2021. doi:10.1101/2021.02.26.21252554

39. Deng X, Garcia-Knight MA, Khalid MM, Servellita V, Wang C, Morris MK, et al. Transmission, infectivity, and antibody neutralization of an emerging SARS-CoV-2 variant in California carrying a L452R spike protein mutation. medRxiv. 2021; 2021.03.07.21252647. doi:10.1101/2021.03.07.21252647

40. Frampton D, Rampling T, Cross A, Bailey H, Heaney J, Byott M, et al. Genomic characteristics and clinical effect of the emergent SARS-CoV-2 B.1.1.7 lineage in London, UK: a whole-genome sequencing and hospital-based cohort study. The Lancet Infectious Diseases. 2021. doi:10.1016/s1473-3099(21)00170-5

41. Teyssou E, Soulie C, Visseaux B, Lambert-Niclot S, Ferre V, Marot S, et al. The 501Y.V2 SARS-CoV-2 variant has an intermediate viral load between the 501Y.V1 and the historical variants in nasopharyngeal samples from newly diagnosed COVID-19 patients. doi:10.1101/2021.03.21.21253498

42. Kow CS, Merchant HA, Hasan SS. Mortality risk in patients infected with SARS-CoV-2 of the lineage B.1.1.7 in the UK. Journal of Infection. 2021. doi:10.1016/j.jinf.2021.05.008

43. Calistri P, Amato L, Puglia I, Cito F, Di Giuseppe A, Danzetta ML, et al. Infection sustained by lineage B.1.1.7 of SARS-CoV-2 is characterised by longer persistence and higher viral RNA loads in nasopharyngeal swabs. International Journal of Infectious Diseases. 2021. pp. 753–755. doi:10.1016/j.ijid.2021.03.005

44. Naveca F, Nascimento V, Souza V, Corado A, Nascimento F, Silva G, et al. COVID-19 epidemic in the Brazilian state of Amazonas was driven by long-term persistence of endemic SARS-CoV-2 lineages and the recent emergence of the new Variant of Concern P.1. 2021 [cited 20 May 2021]. doi:10.21203/rs.3.rs-275494/v1

45. Scientific Advisory Group for Emergencies. NERVTAG: Update note on B.1.1.7 severity, 11 February 2021. GOV.UK; 12 Feb 2021 [cited 21 May 2021]. Available:

https://www.gov.uk/government/publications/nervtag-update-note-on-b117-severity-11-february-2021

46. Funk T, Pharris A, Spiteri G, Bundle N, Melidou A, Carr M, et al. Characteristics of SARS-CoV-2 variants of concern B.1.1.7, B.1.351 or P.1: data from seven EU/EEA countries, weeks 38/2020 to 10/2021. Euro Surveill. 2021;26. doi:10.2807/1560-7917.ES.2021.26.16.2100348

47. Grint DJ, Wing K, Williamson E, McDonald HI, Bhaskaran K, Evans D, et al. Case fatality risk of the SARS-CoV-2 variant of concern B.1.1.7 in England, 16 November to 5 February. Eurosurveillance. 2021;26: 2100256. doi:10.2807/1560-7917.ES.2021.26.11.2100256

48. Challen R, Brooks-Pollock E, Read JM, Dyson L, Tsaneva-Atanasova K, Danon L. Risk of mortality in patients infected with SARS-CoV-2 variant of concern 202012/1: matched cohort study. BMJ. 2021;372. doi:10.1136/bmj.n579

49. Davies NG, Jarvis CI, CMMID COVID-19 Working Group, Edmunds WJ, Jewell NP, Diaz-Ordaz K, et al. Increased hazard of death in community-tested cases of SARS-CoV-2 Variant of Concern 202012/01. medRxiv. 2021. doi:10.1101/2021.02.01.21250959

50. Song Y, Ge Z, Cui S, Tian D, Wan G, Zhu S, et al. COVID-19 cases from the first local outbreak of SARS-CoV-2 B.1.1.7 variant in China presented more serious clinical features: a prospective, comparative cohort study. doi:10.1101/2021.05.04.21256655

51. Louis G, Goetz C, Mellati N, Dunand P, Picard Y. Preliminary data on severe SARS-Cov-2 infection caused by the 501Y.V2 variant. Anaesth Crit Care Pain Med. 2021; 100890. doi:10.1016/j.accpm.2021.100890

52. Ramanathan M, Ferguson ID, Miao W, Khavari PA. SARS-CoV-2 B.1.1.7 and B.1.351 spike variants bind human ACE2 with increased affinity. Lancet Infect Dis. 2021. doi:10.1016/s1473-3099(21)00262-0

53. Collier DA, De Marco A, Ferreira IATM, Meng B, Datir RP, Walls AC, et al. Sensitivity of SARS-CoV-2 B.1.1.7 to mRNA vaccine-elicited antibodies. Nature. 2021;593: 136–141. doi:10.1038/s41586-021-03412-7

54. Tian F, Tong B, Sun L, Shi S, Zheng B, Wang Z, et al. Mutation N501Y in RBD of Spike Protein Strengthens the Interaction between COVID-19 and its Receptor ACE2. bioRxiv. 2021. p. 2021.02.14.431117. doi:10.1101/2021.02.14.431117

55. Laffeber C, de Koning K, Kanaar R, Lebbink JHG. Experimental evidence for enhanced receptor binding by rapidly spreading SARS-CoV-2 variants. bioRxiv. bioRxiv; 2021. doi:10.1101/2021.02.22.432357

56. Cai Y, Zhang J, Xiao T, Lavine CL, Rawson S, Peng H, et al. Structural basis for enhanced infectivity and immune evasion of SARS-CoV-2 variants. bioRxiv. 2021. doi:10.1101/2021.04.13.439709

57. Silva de Souza A, Rivera JD, Almeida VM, Ge P, de Souza RF, Farah CS, et al. Molecular Dynamics Reveals Complex Compensatory Effects of Ionic Strength on the Severe Acute Respiratory Syndrome Coronavirus 2 Spike/Human Angiotensin-Converting Enzyme 2 Interaction. J Phys Chem Lett. 2020;11:

10446–10453. doi:10.1021/acs.jpclett.0c02602

58. Shang J, Ye G, Shi K, Wan Y, Luo C, Aihara H, et al. Structural basis of receptor recognition by SARS-CoV-2. Nature. 2020;581: 221–224. doi:10.1038/s41586-020-2179-y

59. Yi C, Sun X, Ye J, Ding L, Liu M, Yang Z, et al. Key residues of the receptor binding motif in the spike protein of SARS-CoV-2 that interact with ACE2 and neutralizing antibodies. Cell Mol Immunol. 2020;17: 621–630. doi:10.1038/s41423-020-0458-z